Materials Advances

ROYAL SOCIETY OF CHEMISTRY

PAPER

View Article Online
View Journal

Cite this: DOI: 10.1039/d5ma01113b

Magnetic core–satellite Fe/Cu@Zeolite 13X nanocomposite as an efficient catalyst: performance in indigo carmine and tetracycline degradation

Frank Dorinel Solefack Feudjio, [a] Christian Brice Dantio Nguela, [a] Georges Teikam Kenda, [b] Donald Raoul Tchuifon Tchuifon, [c] Roussin Lontio Fomekong, [d] Rhaman Abdoul Ntieche, [ae] Julius Nsami Ndi, *[a] Horace Manga Ngomo *[a] and Cyrille Ghislain Fotsop [b]

To apply the Fenton process to remove organic pollutants from an aqueous solution, catalysts are needed that can decompose hydrogen peroxide (H_2O_2) into hydroxyl radicals and regenerate Fe^{2+} in the system. With this in mind, zeolite-based Fenton-type catalysts were prepared by incorporating Cu_2O and Fe_3O_4 particles into the zeolite X matrix. The core–satellite composite materials (Fe@Zeo13X-1, Fe@Zeo13X-2, Fe/Cu@Zeo13X-1, and Fe/Cu@Zeo13X-2) were synthesized using a hydrothermal-assisted precipitation/co-precipitation method and characterized using X-ray diffraction (XRD), Fourier-transform infrared (FTIR), scanning electron microscopy (SEM), energy dispersive X-ray (EDX) and mapping, electrochemical impedance spectroscopy (EIS), solid UV-visible and N_2 adsorption/desorption. The catalytic properties of the synthesized materials on indigo carmine degradation were evaluated. The results revealed that Fe/Cu@Zeo13X-2 exhibits the greatest catalytic activity, achieving a maximum elimination percentage of 99.96% under the following conditions: pH = 2, 0.2 g L^{-1} of catalyst, 50 mg L^{-1} pollutant, 5 mL of 0.05 M H_2O_2, 60 minutes, and daylight. Irradiating the system with UV radiation highlighted the photocatalytic properties of Fe/Cu@Zeo13X-2, justifying its use in optimizing the photo-Fenton degradation of tetracycline using response surface methodology. A maximum elimination percentage of 94.54% was obtained under the conditions (pH = 6; 1 g L^{-1} of catalyst; 20.92 mg L^{-1} pollutant; 5 mL of 0.5 M H_2O_2; 17.2 min). The first-order kinetics model seems appropriate to describe the degradation kinetics of IC by the Fe/Cu@Zeo13X-2 catalyst ($R^2 > 0.9$). The application of the Langmuir–Hinshelwood (LH) model confirms that the degradation process is limited by adsorption. The material showed good stability, allowing it use over several cycles.

Received 29th September 2025,
Accepted 26th November 2025

DOI: 10.1039/d5ma01113b

rsc.li/materials-advances

1. Introduction

Concerns about aquatic pollution have led to a great deal of work on the use of synthetic zeolites in various processes. This is a class of materials whose popularity is based on their purity and exceptional properties, which include, among others, a large specific surface area, an accessible pore volume and high cation mobility.[1,2] In addition, other properties, such as thermal stability, acid resistivity, hydrophilicity and hydrophobicity can be observed in some zeolites depending on their Si/Al ratio.[3] These properties, which justify the use of these crystalline aluminosilicates of the tectosilicate family in various physicochemical processes such as adsorption,[4,5] ion exchange[6,7] and various catalytic processes,[8–10] result from their particular structures. The latter are made up of a three-dimensional arrangement of tetrahedrons $[SiO_4]^{4-}$ and $[AlO_4]^{5-}$ linked together by oxygen atoms, which gives rise to a porous system made up of regularly connected channels and cages. Among the zeolites, those with a faujasite structure (FAU) are among the most used, particularly zeolite X. This type of zeolite can easily be synthesized from

[a] Laboratory of Applied Physical and Analytical Chemistry, Department of inorganic Chemistry, Faculty of Science, University of Yaoundé 1, P.O. Box 812, Yaoundé, Cameroun. E-mail: bigpielo2002@yahoo.com, ngomo43@yahoo.co.uk
[b] Department of Chemistry, Faculty of Science, Research Unit of Noxious Chemistry and Environmental Engineering, University of Dschang, P.O. Box 67, Dschang, Cameroon
[c] Laboratory of Chemical Engineering and Industrial Bio-Processes (LCEIBP), National Higher Polytechnic School of Douala, University of Douala, P.O. Box 2701, Douala, Cameroon
[d] Department of Chemistry, Higher Teacher Training College, University of Yaounde I, P.O. Box 47, Yaounde, Cameroon
[e] Department of Chemistry, Higher Teacher Training College Bertoua, University of Bertoua, P.O. Box 652, Bertoua, Cameroun

various raw materials that are widely available and inexpensive, such as commercially available silica minerals, fly ash, rice husk ash, and kaolin.[11] The particularity of the zeolite X is also based on its high cation exchange capacity and the presence of large pores materialized by 12-ring windows, which makes it suitable for the elimination of metals and toxic organic molecules in aqueous solution.[7,12]

In the case of organic pollutants, the use of this zeolite involves some methods such as adsorption,[13] ozonation,[14] photocatalysis[15] and Fenton oxidation.[11,16] In its original form, the Fenton process consists of initiating the decomposition of H_2O_2 by Fe^{2+} ions, in order to generate the hydroxyl radical ($^{\bullet}OH$) which is very reactive towards organic compounds.[17] This decomposition can also be achieved by ferric ions and ions from other metals such as Ti, Cr, Mn, Cu, Co and Al in ''Fenton-like'' processes.[18] Although this method is economical from an energy and reagent point of view, and uses non-toxic substances, it is, however, faced with many difficulties, in particular those related to the low pH range, the regeneration of Fe^{2+} ions (slow reaction between Fe^{3+} and $H_2O^{\bullet}$), the recovery of the catalyst and the management of sludge when the latter is precipitated.[18–21] Other limitations of this process lie in the parasitic reactions that can occur between the $^{\bullet}OH$ radicals produced, the reaction intermediates and other molecules present in the reaction medium.[22] In response to these limitations, researchers have turned their attention to heterogeneous processes, using iron oxides, which are easier to recover. However, due to the difficulties linked to the diffusion of H_2O_2 molecules on the surface of these materials, and the ferromagnetic properties of some of these oxides, the catalytic activity has been found to be greatly reduced.[23] To address this, alternatives using supports for the stabilization of metallic species have been proposed by researchers. A very common example is the incorporation of magnetite nanoparticles (Fe_3O_4) into porous materials capable of coupling the oxidation and adsorption processes. This route has been explored by Quynh *et al.*,[23] that obtained a 92.49% removal percentage of methylene blue with a catalyst obtained by incorporating Fe_3O_4 nanoparticles into the structure of a zeolite A. Along the same lines, Fanle *et al.*,[8] obtained a degradation percentage of 95.2% in 15 minutes, by applying a magnetite-zeolite A composite material to the degradation of acid blue-90 by the Fenton process. More recently, Kenda *et al.*,[24] obtained satisfactory results in the degradation of reactive red-198 in aqueous solution by incorporating Fe_3O_4 nanoparticles into the amorphous structure of a biochar derived from orange peels. These authors also showed that the method of modification of the biochar has an impact on the activity of the catalyst, in particular a reduction in the resistance to charge transfer favorable to the rapid formation of $^{\bullet}OH$ radicals using the coprecipitation method. Thus, the biochar modified by the coprecipitation method using an iron(II) and iron(III) salt showed a higher catalytic activity than the catalyst prepared from the iron(II) salt only with an elimination percentage of 98.38% against 95.71%. Other researchers have also exploited the electronic properties of metals to accelerate electron transfer in the reaction medium, in particular by combining iron with a more reducing metal capable not only of accelerating the Fe^{3+}/Fe^{2+} cycle but also of generating $^{\bullet}OH$ radicals from H_2O_2. In view of this, Tchuifon *et al.*,[25] synthesized the composite material $Cu/Fe_2O_3@g\text{-}C_3N_4$ by the doping of graphitic carbon nitride with copper and iron species. The application of this material to the Fenton-type degradation of reactive blue-19 showed exceptional efficiency with a percentage of 96% under optimal conditions (pH = 3, catalyst mass: m = 75 mg, initial pollutant concentration: 100 mg L^{-1} and $[H_2O_2] = 1$ mol L^{-1}). Similar research works have been carried out by Tanga & Wang[26] and Wang *et al.*[27] The former incorporated Cu and Fe nanoparticles into mesoporous carbon (FeCu@C), which degraded 100% of sulfamethazine in 90 min. This result was far superior to that obtained from the iron-doped carbon material (Fe@C), which offered 51.6% removal in 180 min. The results obtained by Wang *et al.*,[27] were more impressive. They doped an iron-based MOF (BUC-96) with copper, which resulted in a material 20.1 times more efficient than the starting MOF, with a degradation percentage of 100% of chloroquine (20 mg) in only 5 minutes. The reduction of Fe^{3+} to Fe^{2+} can also be stimulated by irradiating the reaction medium with ultraviolet radiation. This radiation has another functionality, which lies in its ability to decompose H_2O_2 by photolysis to form $^{\bullet}OH$ radicals.[18] Thus, the development of Fenton-type catalysts with improved optical properties can be an asset for the degradation of organic pollutants in aqueous solution. This idea is very often implemented by constructing heterojunctions between different semiconductors. Heterojunction technology exploits the synergistic interactions between the constituent materials to improve photocatalytic efficiency. S-type architectures are preferred because they minimize charge carrier recombination while maintaining their high redox potential. As a result, the S-type systems developed have a higher photocatalytic capacity than conventional heterojunction photocatalysts.[28–30] As an illustration, Wang *et al.*,[31] synthesized Fe_3O_4/Cu_2O particles with S-type heterojunctions. This material showed excellent catalytic properties in the photo-Fenton degradation of rhodamine B, offering a maximum removal rate of 99.4% under optimal conditions. In this system, when Cu_2O nanoparticles, which are p-type semiconductors, come into contact with Fe_3O_4, which is an n-type semiconductor, a thermodynamic concentration difference results, allowing the migration of photo-induced charge carriers and forming an internal electric field, limiting the recombination of photogenerated electron–hole pairs.[32] The heterojunction between Fe_3O_4 and Cu_2O nanoparticles was also exploited by Liang *et al.*,[33] in the development of the Cu–Fe_3O_4@MIL-101(Fe) composite material. The latter showed excellent photocatalytic activity in the degradation of tetracycline hydrochloride with a removal rate of 96.86%.

This study aims to develop high-performance catalysts that can rapidly regenerate Fe^{2+} ions through two mechanisms: electron exchange between different metal ions and excitation by UV radiation. To achieve this, core–satellite composite materials were developed by doping zeolite X with Cu_2O and Fe_3O_4 (Fe@Zeo13X and Fe/Cu@Zeo13X) in order to remove organic pollutants in aqueous solution by Fenton-type reactions.

This architecture is characterized by the dispersion of metal oxide nanoparticles on the surface of the zeolite, promoting the formation of heterojunctions on the latter. The modification of zeolite was carried out using precipitation and co-precipitation methods in order to evaluate the effect of the modification method on the catalytic properties of the materials. The pollutants studied in this work are tetracycline (TC) and indigo carmine (IC), two substances widely distributed throughout the world. TC is an antibiotic widely used against infectious disease agents and as a growth promoter in livestock.[34,35] Despite its effectiveness against diseases such as bone and joint infections, pneumonia, sexually transmitted infections, skin and gastrointestinal infections, it poses a danger to aquatic species and humans when released into water.[36–40] IC is an anionic dye widely used in the textile industry due to its strong coloration. Its use also extends to medicine, cosmetics and food.[41–43] The risks associated with the presence of this dye in the aquatic environment are numerous, both for fauna and flora, in the sense that it can cause numerous diseases in humans and inhibit certain metabolisms in aquatic plants.[42,44,45] These elements justify the need to eliminate these two molecules from aquatic systems, especially since they are either difficult to degrade or very soluble, which requires the use of specific treatments.[39,40,45,46] Numerous studies have been reported on the degradation of these two pollutants in aqueous solution. This is the case of Muzammal *et al.*,[47] who carried out the green synthesis of an Nd_2O_3 catalyst for the photocatalytic degradation of TC, Benedoue *et al.*,[48] who studied the photocatalytic degradation of IC by functionalized carbon nitride, and Bopda *et al.*,[49] who developed a ferromagnetic biochar for the Fenton degradation of IC. The study of the degradation of these organic pollutants will involve evaluating the effect of different experimental parameters including pH, catalyst mass, initial pollutant concentration, contact time and H_2O_2 concentration on the removal efficiency. Given the resistance of TC to degradation, the optimal conditions for its removal were determined by the Response Surface Methodology (RSM) using the central composite design (CCD) in a photo-Fenton process.

2. Materials and methods

2.1. Reagents

Several reagents from various sources were used in this study. For this purpose, $FeSO_4{\cdot}7H_2O$, $FeCl_3{\cdot}6H_2O$ and $CuSO_4{\cdot}5H_2O$ were all supplied by GHTECH (Guangdong Guanghua Sci-Tech Co. Ltd, China). NaOH and colloidal silica solution were supplied by Merk. HCl was supplied by JHD (Guangdong Guanghua Sci-Tech Co. Ltd, China). TC was supplied by Sigma Aldrich (Germany) while IC was supplied by PROBUS SA BADALONA (Barcelona, Spain). The main source of silica and alumina used in the synthesis of zeolite was kaolin, collected in the South region of Cameroon. After collection, the kaolin was sieved through pores smaller than 25 μm and then used without pretreatment.

2.2. Hydrothermal synthesis of zeolite Na-X

The synthesis of zeolite X began with the thermal activation of kaolin at 1173 K. The obtained metakaolin (MK), which is more reactive than kaolin, was used to prepare an alumina silicate solution by dissolving it in 12.5 mL of NaOH (4 M). A colloidal gel solution, obtained by dissolving 12 mL of a colloidal silica solution in 12.5 mL of NaOH (4 M), was then added dropwise to the alumina silicate solution. The resulting mixture was homogenized by stirring for 5 hours, before being aged for 24 hours at room temperature without stirring. The gel was subsequently subjected to a crystallization step at 373 K for 8 hours. After cooling, the suspension obtained was washed several times and filtered. The final product, named Zeo13X, was obtained after drying the residue at 363 K.

2.2.3. Synthesis of Fe@Zeo13X. The synthesis of Fe@Zeo13X was carried out by modifying the Zeo13X material by the precipitation method using two routes: the precipitation of an Fe(II) salt and the co-precipitation of Fe(II) and Fe(III) salts in the presence of NaOH, used as a precipitating agent. Thus, two metal salt solutions (S_1) and (S_2) were prepared. For (S_1) 5g of $FeSO_4{\cdot}7H_2O$ were dissolved in in 150 mL of distilled water while for (S_2), 5 g of $FeSO_4{\cdot}7H_2O$ and 5g of $FeCl_3{\cdot}6H_2O$ were dissolved in the same volume of distilled water. Subsequently, in two different Erlenmeyer flasks, the solutions (S_1) and (S_2) were each mixed with 5 g of NaOH, then stirred for 15 min at 353 K at a speed of 625 rpm. After 15 min of stirring, 5 g of zeolite were added to each mixture and the whole mixture was kept under agitation for 90 min under the same conditions. After cooling to room temperature, the final solutions were centrifuged and the solid residues obtained were washed several times and then dried at 363K for 24 hours. The materials obtained using (S_1) and (S_2) were named Fe@Zeo13X-1 and Fe@Zeo13X-2, respectively.

2.2.4. Synthesis of Fe/Cu@Zeo13X. The synthesis of Fe/Cu@Zeo13X was carried out by co-precipitation of Fe(II), Fe(III) and Cu(II) salts onto the zeolite matrix, a process similar to that used for Fe@Zeo13X. In this case, solutions (S_1) and (S_2) were replaced by two solutions (S_3) and (S_4). Solution (S_3) was prepared by dissolving 5 g of $FeSO_4{\cdot}7H_2O$ and 5 g of $CuSO_4{\cdot}5H_2O$ in 150 mL of distilled water while (S_4) was prepared by dissolving 5 g of $FeSO_4{\cdot}7H_2O$, 5 g of $FeCl_3{\cdot}6H_2O$ and 5 g of $CuSO_4{\cdot}5H_2O$ in the same volume of distilled water. The materials from (S_3) and (S_4) were named Fe/Cu@Zeo13X-1 and Fe/Cu@Zeo13X-2, respectively.

2.3. Characterization techniques

A multitude of analytical techniques were used to verify the physicochemical properties of the synthesized materials, including scanning electron microscopy (SEM) coupled with energy-dispersive X-ray spectroscopy (EDX), UV-visible spectroscopy, powder X-ray diffraction (XRD), Fourier transform infrared spectroscopy (FT-IR), electrochemical impedance spectroscopy (EIS), and N_2 adsorption/desorption. A TESCAN VEGA 3-LMU instrument operating at 8 kV was used for SEM and EDX analyses. Before SEM-EDX analysis, the samples were mounted on aluminum supports and coated with thin layers of sputtered

gold to make them conductive. Electrochemical impedance spectroscopy (EIS) was performed using a CORRTEST potentiostat (CS310M) in the frequency range of 10 mHz to 100 kHz, with an AC signal of amplitude 10 mV peak-to-peak, at a potential of −0.25 V. The electrolyte used was a Na_2SO_4 solution (10 g L^{-1}). An analytical powder diffractometer PAN XPERT Pro, automated with Cu-$K_{\alpha 1}$ radiation filtered at the anode, was used to record the diffraction patterns of the materials. The radiation wavelength was (λ) = 1.54056 Å, the accelerating voltage was 40 kV at 40 mA, the 2θ range was 4–90°, and the time constant was 27.5400 s with a step interval (2θ per step) of 0.0260. A Jasco V750 UV-visible spectrophotometer equipped with an integrating sphere, in absorbance mode was used to evaluate the optical properties of the samples. The measurements were performed in continuous scanning mode between the wavelength range of 200 and 800 nm with a scanning speed of 400 nm min^{-1}. FT-IR spectroscopy in attenuated total reflection mode was used to determine the surface functional groups of the materials. A Nicolet Thermoscientific IS5 spectrophotometer was used for this purpose, with spectra recorded in the range of 4000 to 400 cm^{-1}. A BELSORP MAX instrument from Bel Japan Inc. was used to determine the textural properties of the materials, including the specific surface area, pore size, and volume of the materials from N_2 adsorption/desorption isotherms using BET/BJH models.

2.4. Degradation of IC

Before proceeding with the degradation of TC, the catalytic properties of the materials were evaluated using them to degrade IC in an aqueous solution. Batch mode degradation tests were carried out by introducing 50 mg of catalyst and 5 mL of H_2O_2 (0.02 M) into an Erlenmeyer flask containing 250 mL of an IC solution (50 mg L^{-1}) at pH = 2. The whole was then stirred using a magnetic stirrer and 5 mL samples were taken at increasing time intervals of 5, 10 and then 20 min, before filtering. After each filtration, two drops of methanol were added to the filtrate to stop the reaction. Then, the concentration of the dye at equilibrium was determined by measuring it with a SPECTRUMLAB S-23A UV-visible spectrophotometer at a wavelength of 610 nm. For each sample, the IC removal efficiency was calculated using eqn (1) below:

$$R = \frac{C_0 - C_e}{C_0} \times 100 \quad (1)$$

where C_e is the equilibrium concentration, C_0 the initial concentration and R the percentage removal of the pollutant.

For the Fe/Cu@Zeo13X-2 catalyst that demonstrated the best degradation performance, the experiments were repeated by varying the experimental conditions, in order to evaluate the effects of different factors on the degradation process. Thus, in addition to the reaction time, the effect of pH (2–8), H_2O_2 concentration (0–0.05 M), mass (10–50 mg), IC concentration (20–50 mg L^{-1}) and UV radiation (60 W m^{-2}, λ_{max} = 365 nm) on the removal efficiency were studied.

2.5. Modeling of TC degradation on Fe/Cu@Zeo13X-2 catalyst

The modeling and optimization of TC degradation from the Fe/Cu@Zeo13X-2 catalyst was performed using the response surface methodology (RSM). For this purpose, a four-factor centered composite design (CCD) predicted 27 experiments to be performed (eqn (2)), in which the response is the TC removal efficiency. All experiments were carried out in the presence of an UV light source (18 W m^{-2}, λ_{max} = 365 nm). For each experiment, a volume of 50 mL of TC and 5 mL of 0.5 M H_2O_2 were used. At the end of each experiment, the residual antibiotic concentration was evaluated by spectrophotometric assay at 356 nm. Table 1 presents the coded or real experimental variables, whose influence on TC degradation kinetics was studied, while specifying their respective variation domains. These parameters, along with their interactions, were related to the removal efficiency using the quadratic relationship given by eqn (3).

$$N = 2^k + 2k + n = 2^4 + 2 \times 4 + 3 = 27 \quad (2)$$

where k represents the number of experimental variables, n the number of points in the center of the domain and N the total number of experiments to be carried out.

$$R = b_0 + \sum_{i=1}^{4} b_i X_i + \sum_{i=1}^{4} b_{ii} X_i^2 + \sum_{i=1}^{4} \sum_{j=1}^{4} b_{ij} X_i X_j + \varepsilon \quad (3)$$

where R is the theoretical value of the response; X_i the coded variable corresponding to the factor i; b_0 the theoretical value of the response at the center of the experimental domain; b_i the coefficient of the linear terms; b_{ij} the coefficient measuring the interaction effect between the factors i and j; b_{ii} the coefficient of the quadratic terms and ε the error between the measured and predicted values.

Degradation kinetics

The reaction kinetics associated with the degradation of IC and TC were studied by fitting first- and second-order kinetic models to experimental data obtained under optimal conditions. This fitting was carried out using the linear regression method. The linear and non-linear forms associated with these models are shown in Table 2.

In these equations, C_0 (mg L^{-1}) and C_t (mg L^{-1}) denote the initial concentration and the concentration of the pollutant at time t of the reaction, respectively, while k and k' are the reaction rate constants.

Table 1 Factors and their range of variation

		Range and levels		
Name	Units	−1	0	+1
A: pH	—	3	6	9
B: TC concentration	mg L^{-1}	5	15	25
C: Mass	mg	10	30	50
D: Time	min	5	15	25

Table 2 Linear and nonlinear forms of kinetic models

Model	Non-linear form	Linear form	
First order	$-\frac{dC}{dt} = kC$	$\ln\frac{C_0}{C_t} = kt$	(4)
Second order	$-\frac{dC}{dt} = k'C^2$	$\frac{1}{C_t} - \frac{1}{C_0} = k't$	(5)

3. Results and discussion

3.1. Characterization of materials

3.1.1. X-ray diffraction and FTIR analysis. The identification of the crystalline phases present in the materials was carried out by XRD analysis, the results of which are illustrated in Fig. 1a. On the XRD pattern of Zeo-13X, the observed diffraction lines at 6.10, 9.99, 11.72, 15.37, 18.43, 20.08, 22.48, 23.30, 26.61, 29.22, 30.35, 30.97, 31.97, 33.59, 34.19 and 37.37° which can be attributed to the (111), (220), (311), (331), (511), (440), (620), (533), (642), (733), (822), (555), (840), (664), (931) and (666) planes respectively, correspond to the data of JCPDS sheet no 12-0228, characteristic of X-type faujasite. This observation could be considered as an indicator of a successful hydrothermal synthesis. These characteristic lines remain visible on the XRD patterns of the modified samples, suggesting that the structure of the zeolite is preserved after post-synthetic treatments.[5] On the other hand, the modification causes a significant reduction in the crystallinity of the zeolite, as suggested by the significant attenuation of the diffraction lines on the XRD patterns of the modified samples. For this purpose, the crystallinity index obtained with the Match! 3 software was evaluated at 30.34% for Zeo13X and at 4.85, 5.63, 5.53, and 4.76% for Fe@Zeo13X-1, Fe@Zeo13X-2, Fe/Cu@Zeo13X-1 and Fe/Cu@Zeo13X-2, respectively. This reduction in crystallinity is correlated with a significant change in crystallite size, as shown by the average crystallite size values calculated by the Scherrer formula (eqn (6)) for each sample (Table 3). Furthermore, the characteristic iron and copper oxide lines are not easily identifiable in these composite materials, probably due to the high proportion of zeolite X, whose strong intensity of diffraction lines contributes to masking those of these oxides. However, the presence of magnetite (JCPDS card no. 01-088-0315) is illustrated by the appearance of a low intensity line around 35.7°, visible on the XRD patterns of Fe@Zeo13X-2 and Fe/Cu@Zeo13X-1. In addition, the Fe/Cu@Zeo13X-1 sample exhibits a diffraction line at 38.69°, which can be attributed to the cuprite phase (JCPDS no. 65-3288).[50,51] These results suggest that during the modification, nanoparticles of these metal oxides were formed on the surface of the zeolite.

$$D = \frac{K\lambda}{\beta\cos\theta} \quad (6)$$

where D is the crystallite size, K is a geometric factor taken as 0.9, λ is the X-ray wavelength, θ is the diffraction angle and β is the full width at half maximum of the diffraction peak at 2θ.

The results of the FTIR (Fig. 1b) spectroscopic analyses are in perfect agreement with those of the XRD. Indeed, the characteristic bands of zeolite X are visible on the Zeo13X sample and its modified forms. These include the intense band located between 1000 and 850 cm^{-1}, and that located between 689 and 669 cm^{-1}, which are characteristic of the asymmetric internal Si–O and Al–O bonds of the tetrahedral $[SiO_4]^{4-}$ and $[AlO_4]^{5-}$.[4,52] The band between 1648 cm^{-1} and 1644 cm^{-1} is associated with the presence of physisorbed water molecules, while the one observed around 3350 cm^{-1} reveals the presence of water molecules bound to the zeolite structure. In addition, the bands between 751 and 775 cm^{-1} are attributed to the symmetric stretching vibration mode of the O–Si–O and O–Al–O groups, while those between 558 and 571 cm^{-1} can be attributed to the Si–O and Al–O bonds of the six-membered rings.[52,53] However, the incorporation of Cu_2O and Fe_3O_4 leads to slight structural modifications, illustrated by the appearance of new adsorption bands, characteristic of Fe–O and Cu–O bonds. To this end, the characteristic bands of Fe–O bonds were observed between 628 and 635 cm^{-1} on the spectra of all the modified samples,[54] while those characteristic of Cu–O bonds were observed at 1085, 869, 770 and 730 cm^{-1},[55–57] on the spectra of the Fe/Cu@Zeo13X-1 and Fe/Cu@Zeo13X-2 samples. The presence of iron and copper oxides in the zeolite structure

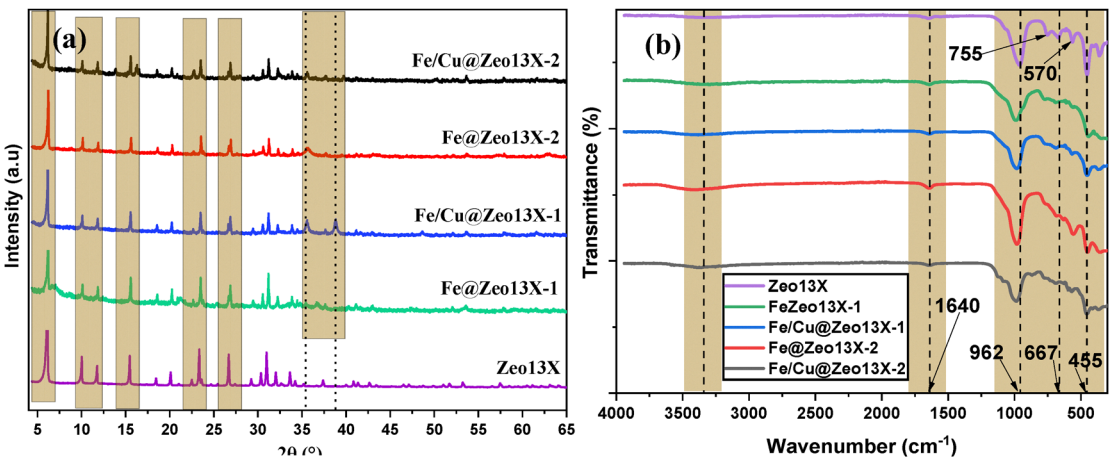

Fig. 1 XRD pattern (a) and FTIR (b) analyses of Zeo13X, Fe@Zeo13X-1, Fe@Zeo13X-2, Fe/Cu@Zeo13X-1 and Fe/Cu@Zeo13X-2.

Table 3 Crystallinity of samples

Sample	Crystallinity index (%)	Average crystallite size (Å)
Zeo13X	30.3	1849.9
Fe@Zeo13X-1	4.85	3283.2
Fe@Zeo13X-2	5.63	13 265.7
Fe/Cu@Zeo13X-1	5.53	167 485.8
Fe/Cu@Zeo13X-2	4.76	1957.9

causes a shift of the band centered between 986 and 976 cm^{-1}, characteristic of Si–O and Al–O bonds, towards higher wavenumbers. This shift is more accentuated in copper-doped materials. These observations suggest the effective incorporation of iron and copper oxides in the structure of zeolite X.

3.1.2. SEM and EDX/EDX-mapping analysis. The morphology of the samples given by SEM is represented by Fig. 2a. According to the results obtained, the post-synthetic modification leads to a significant alteration of the morphology of the starting 13X zeolite. While the latter presents uniform particles, the modified samples present particles of different sizes, mostly smaller than those of the starting zeolite. This observation could be linked to the melting of the zeolite due to the high concentration of NaOH in the reaction medium. In addition, large agglomerations of particles are also visible on the modified samples, showing the formation of core–satellite materials. These results are in perfect agreement with the XRD results. Furthermore, the EDX elemental analysis (Fig. 2b), reveals that the Zeo13X sample has a surface essentially made up of the elements Si, Al, O and Na, which could be an indicator of the purity of the synthesized zeolite. The modification of this zeolite leads to the appearance of Cu and Fe elements on the surface of the Fe/Cu@Zeo13X-1 and Fe/Cu@Zeo13X-2 samples on the one hand and of the Fe element on the surface of the Fe@Zeo13X-1 and Fe@Zeo13X-2 samples on the other hand. These elements, whose presence in the composite materials could be an indication of the success of the modification process, are however distributed heterogeneously on the surface of these materials as indicated by the images obtained by EDX mapping (Fig. 2b). This observation could result from a potential accumulation of metallic species in the pores of the zeolite X during the post-synthetic treatment, giving rise to regions rich in Fe and Cu.

EDX data reveal, unsurprisingly, a high presence of iron on the surface of the Fe@Zeo13X-1 and Fe@Zeo13X-2 samples. This atomic proportion is higher on the surface of Fe@Zeo13X-2 with an estimated value of 19%. This result is undoubtedly related to the high mass of ferrous and ferric salt used during its preparation. The same reason could be sufficient to justify the high Fe content observed on the surface of Fe/Cu@Zeo13X-2 (15%) compared to Fe/Cu@Zeo13X-1 (10%). However, the presence of copper contributes to reduce this proportion of iron compared to Fe@Zeo13X-1 and Fe@Zeo13X-2. Since the decomposition of H_2O_2 by the Cu^{2+}/Cu^{+} system (eqn (7) and (8)) is slower than that using the Fe^{3+}/Fe^{2+} system (eqn (9) and (10)),[58] this difference in proportion can substantially influence the catalytic activity of the different materials.

$$Cu^{+} + H_2O_2 \rightarrow Cu^{2+} + HO^{\bullet} + HO^{-} \quad (7)$$

$$Cu^{2+} + H_2O_2 \rightarrow Cu^{+} + HO_2^{\bullet} + H^{+} \quad (8)$$

$$Fe^{2+} + H_2O_2 \rightarrow Fe^{3+} + HO^{\bullet} + HO^{-} \quad (9)$$

$$Fe^{3+} + H_2O_2 \rightarrow Fe^{2+} + HO_2^{\bullet} + H^{+} \quad (10)$$

3.1.3. UV-visible analysis of the catalysts. The optical properties of the samples determined from UV-visible spectroscopy reveal that the incorporation of Cu_2O and Fe_3O_4 nanoparticles into the zeolite structure leads to a considerable improvement in light absorption (Fig. 3a). This improvement is correlated with a shift of the absorption edge in the visible domain. Furthermore, as shown by the Tauc plot ($(\alpha h\nu)^2 = f(h\nu)$) represented in Fig. 3b, the presence of metal oxides leads to a significant reduction in the band gab energy, from approximately 4.11 eV for Zeo13X to 2.28, 1.73, 1.82 and 1.94 eV for Fe@Zeo13X-1, Fe/Cu@Zeo13X-1, Fe@Zeo13X-2 and Fe/Cu@Zeo13X-2. This reduction is greater for samples modified by coprecipitation, suggesting that the simultaneous use of several metal salts leads to a greater reduction in the charge recombination rate. These results suggest the idea of an improvement in the catalytic properties of the materials following the applied post-synthetic treatment. Similar results were observed by Liang *et al.*[33] Furthermore, the reduction in band gap energy observed in the iron-modified samples (Fe@Zeo13X-1 and Fe@Zeo13X-2) suggests that this metal plays a key role in reducing the charge recombination rate. However, the addition of copper leads to a reduction in this energy (comparison between Fe@Zeo13X-1 and Fe/Cu@Zeo13X-1) on the one hand, and an increase (comparison between Fe@Zeo13X-2 and Fe/Cu@Zeo13X-2) on the other. This observation suggests that the reduction in band gap energy cannot be associated with the effect of a single metal, but rather with the synergistic effect between iron and copper oxides. Indeed, the formation of a heterojunction between these two oxides can lead to improved optical properties while reducing the recombination rate of photogenerated charges.[32]

3.1.4. Electrochemical impedance spectroscopy. EIS analysis was used to characterize the separation and recombination of charge carriers within the composite materials. The results obtained allowed to plot the Nyquist and Bode diagrams (Fig. 3c and d). Nyquist plots is an essential tool for visually comparing the charge transfer resistances of different samples. In this type of plot, it is established that the value of the charge transfer resistance is determined by the radius of the arc observed. Thus, an increase in the size of the arc radius leads to increased charge transfer resistance.[59,60] In this context, the Fe/Cu@Zeo13X-2 material exhibits the lowest resistance to photoexcited electron transfer, which could indicate better catalytic properties compared to other catalysts.[61] This result suggests that there is little resistance to electron exchange between the Fe^{2+}, Fe^{3+}, and Cu^{+} ions present in this material. Simulation of the EIS data using the equivalent circuit shown in Table 4 confirmed this observation, providing estimates of the charge transfer resistances. The values obtained for the Zeo13X,

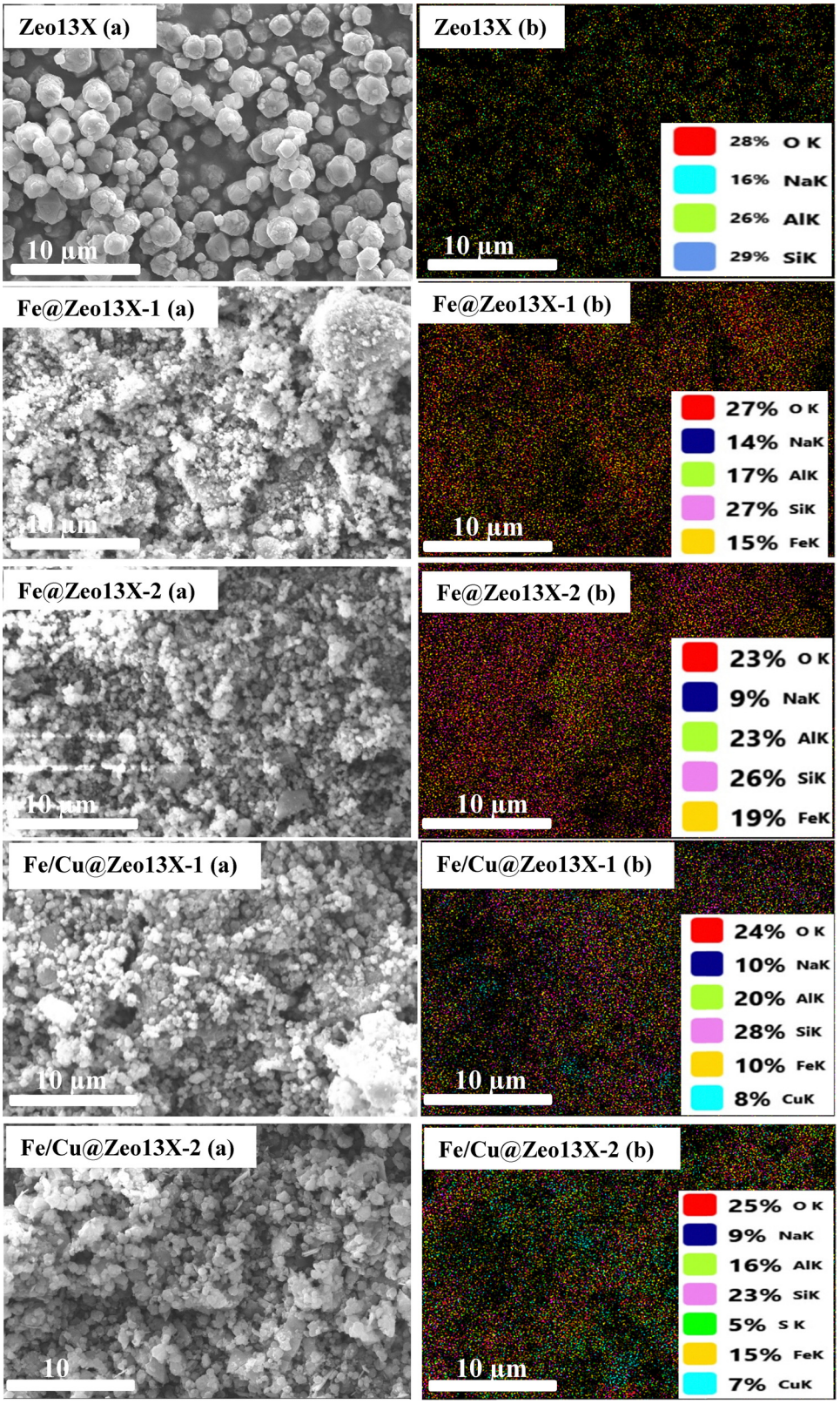

Fig. 2 Morphology given by SEM (a) and EDX mapping (b) of the catalysts.

Fe@Zeo13X-1, Fe@Zeo13X-2, Fe/Cu@Zeo13X-1, and Fe/Cu@Zeo13X-2 samples are 43798.14, 6902.05, 46613.24, 57945.67, and 6232.31 Ω, respectively. However, the incorporation of magnetite into the matrix by simple precipitation of an iron(II)

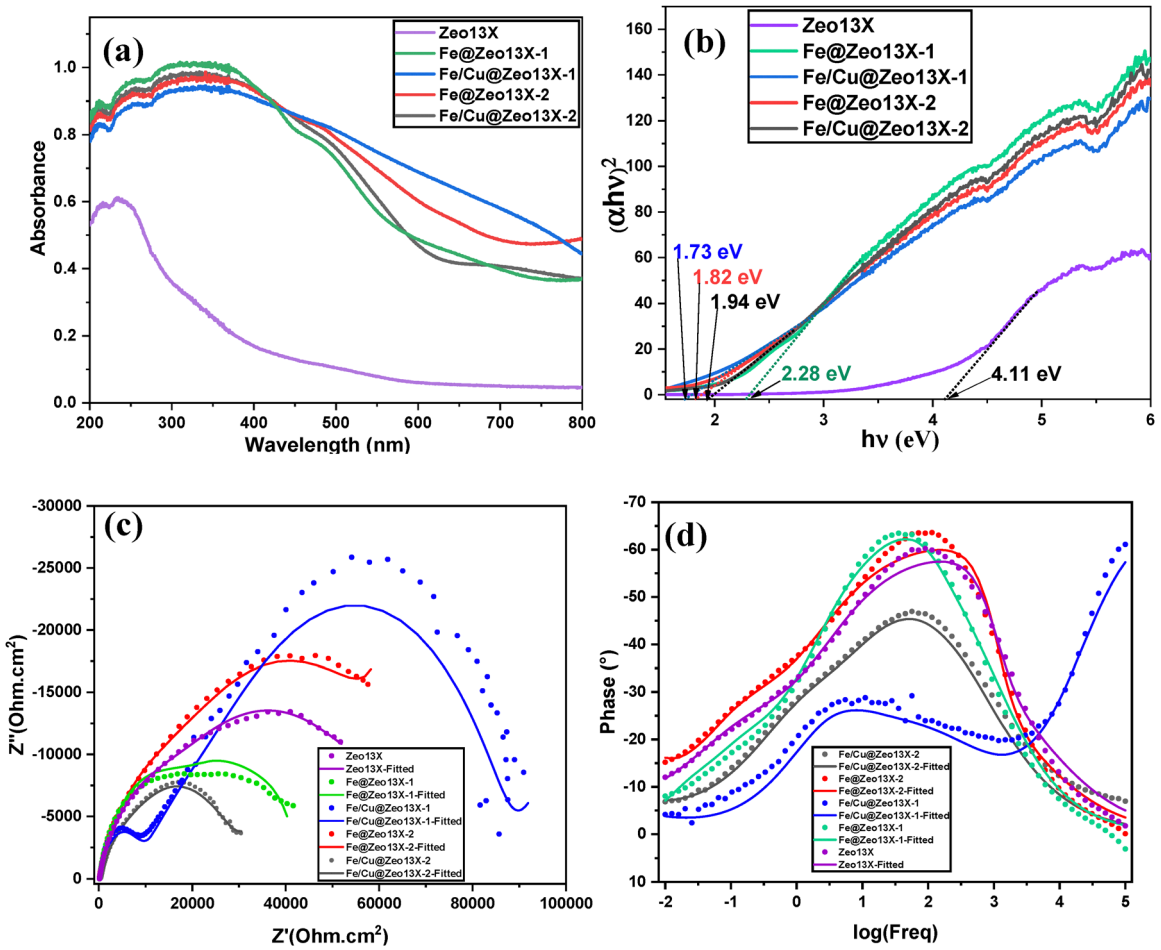

Fig. 3 UV-visible analysis of samples (a); Tauc plot (b); Nyquist diagrams (c); Bode diagrams (d).

Table 4 Modeling of the equivalent EIS circuit and charge transfer resistance

Sample	Charge transfer resistance (kΩ)	Equivalent circuit
Zeo13X	43.80	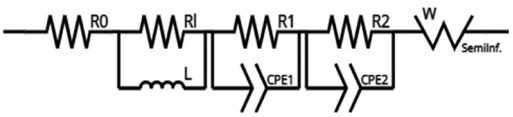
Fe@Zeo13X-1	6.90	
Fe@Zeo13X-2	46.61	
Fe/Cu@Zeo13X-1	57.95	
Fe/Cu@Zeo13X-2	6.23	

salt further improves conductivity compared to the coprecipitation method, which contradicts the observations of Kenda *et al.*[24] In addition, the high resistance of Fe/Cu@Zeo13X-1 could be indicative of a lower catalytic activity than the other materials. The τ_e values of the charge carrier lifetime were evaluated from the relation (11), where f_{max} is the maximum frequency,[62] given by the Bode plots (Fig. 3d).

$$\tau_e = \frac{1}{2\pi f_{max}} \quad (11)$$

The results (Table 5) obtained show that the lifetime of charge carriers in the Fe@Zeo13X-1 catalyst is the highest with an estimated value of 4.49 ms, suggesting a low rate of charge recombination of electrons of this material in the electrolyte used.[63] In addition, the Fe/Cu@Zeo13X-2 catalyst has a higher τ value than the other samples. These results suggest that the Fe@Zeo13X-1 and Fe/Cu@Zeo13X-2 samples could present the best catalytic activities among the samples used. Moreover, in addition to its high resistance to charge transfer, the Fe/Cu@Zeo13X-1 catalyst has a low lifetime of charge carriers,

Table 5 Crystallinity of samples

Sample	f_{max} (Hz)	τ_e (ms)
Zeo13X	89.125	1.79
Fe@Zeo13X-1	35.481	4.49
Fe/Cu@Zeo13X-1	100 000	1.59×10^{-3}
Fe @Zeo13X-2	114.815	1.39
Fe/Cu@Zeo13X-2	70.795	2.25

which supports the idea that it could present the lowest catalytic activity.

3.1.5. Adsorption/desorption of N_2. The evaluation of the textural properties of the samples reveals a significant reduction in the amount of adsorbed N_2 (Fig. 4a), probably due to the accumulation or agglomeration of metal oxide nanoparticles in the pores of the modified materials, which prevents the diffusion of atoms of these molecules. This results in a drastic decrease in the BET surface area with a change from 624 $cm^2\ g^{-1}$ for the Zeo13X sample to 161, 123, 377 and 270 $cm^2\ g^{-1}$ for Fe@Zeo13X-1, Fe/Cu@Zeo13X-1, Fe@Zeo13X-2 and Fe/Cu@Zeo13X-2 respectively. This observation is correlated with a significant reduction in the pore volume as illustrated in Table 6. Similar observations were reported by Ngomade *et al.*,[10] when incorporating ZrO_2 nanoparticles into the structure of a MFI structural type zeolite. Moreover, the reduction of BET surface area and pore volume could be accompanied by the formation of mesopores in Fe@Zeo13X-1 and Fe/Cu@Zeo13X-1 materials, as illustrated by the transition from a type I isotherm for Zeo13X to a type IV isotherm, characterized by H4 type hysteresis for these two materials (Fig. 4b).[64] In this context, pore obstruction is identified as a factor limiting the diffusion of large molecules, such as IC and TC, to active sites located inside the pores. However, the core–satellite architecture of composite materials is characterized by the dispersion of metal oxide nanoparticles across the entire surface of the zeolite particles, which constitute the central element.[65] This configuration ensures that target molecules are accessible to the nanoparticles, which constitute the active phase of the composite materials, thereby promoting effective interactions between these two entities.

3.2. Application to the degradation of IC in aqueous solution

3.2.1. Evaluation of the catalytic activity of the materials. In order to determine the impact of the modification processes on the catalytic properties of the samples, the latter were applied to the Fenton-type degradation of the IC dye, under the conditions described in paragraph 2.4. The data obtained, visualized in Fig. 5a, demonstrate that the treatments carried out significantly improve the catalytic properties of the zeolite, with respective removal percentages of 96.90, 87.34, 97.42 and 98.70% for Fe@Zeo13X-1, Fe/Cu@Zeo13X-1, Fe@Zeo13X-2 and Fe/Cu@Zeo13X-2 in 60 min, compared to 25.55% for Zeo13X. The efficiency of these composite materials is further confirmed by the low removal efficiency obtained by reacting 5 mL of hydrogen peroxide (0.02 M) with 250 mL of IC dye solution (50 mg L^{-1}, pH = 2) in the absence of material in daylight. On the other hand, as predicted by the EIS analysis results, the Fe/Cu@Zeo13X-2 sample showed the best catalytic activity. This material stands out from other samples probably by the high Fe content on its surface to which is associated a significant proportion of Cu capable of accelerating the regeneration of Fe^{2+} from Fe^{3+} according to eqn (12).[49,66] This idea is based on the relatively low redox potential of the Cu^{2+}/Cu^{+} couple, estimated at 0.153 V, compared to the Fe^{3+}/Fe^{2+} couple, estimated at 0.77 V. This difference in potential favors the reduction of Fe^{3+} to Fe^{2+}. Thus, the incorporation of Fe_3O_4 and Cu_2O nanoparticles by coprecipitation of Fe(II), Fe(III) and Cu(II) salts constitutes the best alternative for obtaining a Fenton-type catalyst for the degradation of organic pollutants in aqueous solution. For this reason, the effect of different factors on the degradation efficiency of IC by the Fe/Cu@Zeo13X-2 catalyst was evaluated.

$$Cu^{+} + Fe^{3+} \rightarrow Cu^{2+} + Fe^{2+} \quad (12)$$

3.2.2. Effect of different parameters on IC degradation by Fe/Cu@Zeo13X-2. H_2O_2 concentration, catalyst mass and IC

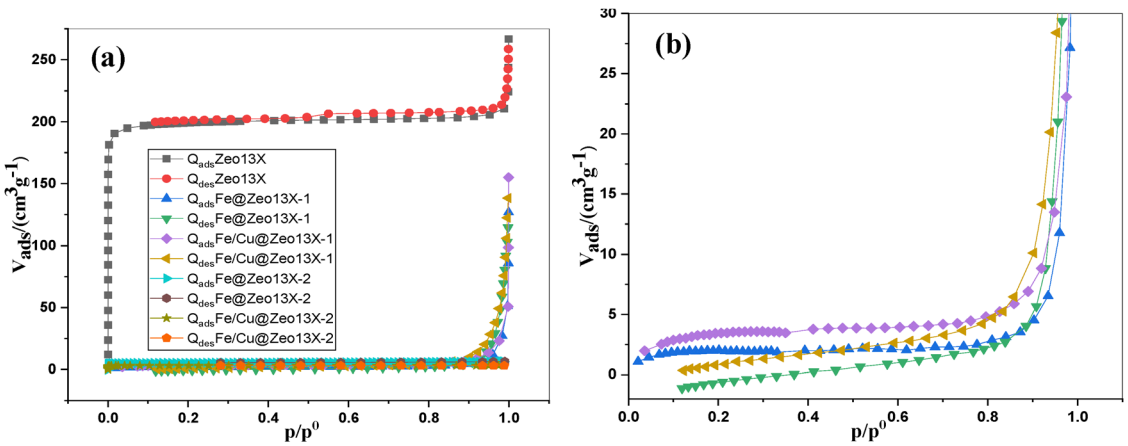

Fig. 4 BET (a) and BJH (b) analysis of Fe@Zeo13X-1, Fe/Cu@Zeo13X-1, Fe@Zeo13X-2 and Fe/Cu@Zeo13X-2.

Table 6 Textural properties of samples

	Zeo13X	Fe@Zeo13X-1	Fe/Cu@Zeo13X-1	Fe@Zeo13X-2	Fe/Cu@Zeo13X-2
S_{BET} ($cm^2\ g^{-1}$)	624	161	123	377	270
Mean pore volume ($cm^3\ g^{-1}$)	0.31	0.01	0.02	0.25	0.11

solution concentration on the degradation percentage were evaluated at room temperature conditions in the presence of daylight to determine the optimal degradation conditions. For this purpose, the influence of solution pH was studied by placing 50 mg of Fe/Cu@Zeo13X-2 catalyst in contact with 250 mL of IC solution (50 mg L^{-1}) and 5 mL of H_2O_2 (0.02 M) at different pH (2, 3, 4, 6 and 8). The results obtained, shown in Fig. 5b, indicate the evolution of the removal efficiency for different pH values. These results show a high catalytic activity for pH values equal to 2 and 3, with faster degradation kinetics at pH = 2. According to the results obtained, increasing the pH from 2 to 8 leads to a reduction in the efficiency of the material. Similar observations were made by Ahmad *et al.*,[67] during the Fenton-type degradation of ofloxacin by a zeolite loaded with magnetite nanoparticles. This trend could result from the favorable interactions that exist between the IC molecules and the catalyst at low pH values. Indeed, the pH at the zero charge point of the Fe/Cu@Zeo13X-2 catalyst was evaluated at 7.86 (Fig. 5c), which suggests the existence of attractive interactions between the anionic IC dye and the positively charged surface of this catalyst for pH values lower than 7.86. These interactions are progressively reduced as the pH increases, due to the progressive reduction of positive charges on the catalyst surface, which finally becomes negative for pH values higher than 7.86. These results highlight the essential role of the adsorption process in Fenton-type catalytic processes in heterogeneous phase.

The effect of catalyst mass was studied between 10 and 50 mg at pH = 2, while keeping constant the other experimental conditions previously defined during the study of the influence of pH. The results (Fig. 5d) obtained show a considerable acceleration of the degradation when the catalyst load increases, giving removal percentages of 77.77, 88.27, 96.42, 98.42 and 98.74% in 60 min for 10, 20, 30, 40 and 50 mg of catalyst respectively. This trend may be linked to the combination of adsorption and oxidation effects. Indeed, an increase in the catalyst mass can lead to a multiplication of active sites, leading to an increase in effective collisions between the catalyst and the molecules present in solution.[67,68] This results in an acceleration of the decomposition of H_2O_2 and therefore of the degradation of the dye. However, the maximum elimination percentage evaluated at 99.18% is obtained for a catalyst mass of 30 mg after 80 min of reaction, probably due to the capture of $^{\bullet}OH$ radicals by the iron species present on the surface of the catalyst, when the mass of the latter is greater, which inhibits the catalytic activity.[69]

As the main source of $^{\bullet}OH$ radicals, H_2O_2 is of paramount importance for Fenton-type reactions. Therefore, a rigorous analysis of the impact of its concentration on the catalytic performance is essential. In this perspective, the effect of H_2O_2 concentration was evaluated by maintaining the catalyst mass at 50 mg, the pH at 2, the dye volume at 250 mL at a concentration of 50 mg L^{-1} and the H_2O_2 volume at 5 mL. The results shown in Fig. 6a illustrate the evolution of IC degradation at different H_2O_2 concentrations. As a result, increasing the hydrogen peroxide concentration from 0.005 M to 0.02 M induces a substantial improvement in the degradation process, with removal percentages of 68.85, 80.87 and 98.74% in 60 min at 0.005, 0.01 and 0.02 M respectively. However, beyond 0.02 M, the removal efficiency increases only marginally, with a value estimated at and 99.96% in 60 min at 0.05 M. These are in perfect agreement with the literature data.[70–72]

The rapid increase in the removal efficiency can be attributed to the insufficiency of $^{\bullet}OH$ radicals at low H_2O_2 concentration and their progressive increase with increasing concentration. However, when the concentration becomes too high, the excess H_2O_2 acts as a radical scavenger for $HO^{\bullet}$, leading to the formation of hydroperoxyl radicals $HO_2^{\bullet}$, according to eqn (13).[67,73] Furthermore, the low removal efficiency in the absence of H_2O_2 confirms the predominant role of the latter in the process studied.

The study of the influence of the initial dye concentration was evaluated between 20 and 50 mg L^{-1}. For each experiment, the pH of the dye solution at the appropriate concentration was adjusted to 2, and the other parameters were maintained in the experimental conditions previously defined during the study of the influence of pH. The results obtained (Fig. 6b), show a decrease in the degradation rate when the concentration increases. This observation can be attributed to the saturation of the active sites at high dye concentrations. Similar results were obtained by Moosavifar *et al.*[74]

$$HO^{\bullet} + H_2O_2 \rightarrow H_2O + H_2O^{\bullet} \quad (13)$$

3.2.3. Evaluation of photocatalytic properties of Fe/Cu@Zeo13X-2 catalyst. The evaluation of the photocatalytic properties of the Fe/Cu@Zeo13X-2 catalyst was carried out through photo-Fenton degradation experiments under UV irradiation. For this, 250 mL of an IC solution (50 mg L^{-1}) pH = 2 was treated in the presence of 50 mg of the catalyst and 5 mL of H_2O_2 (0.05 M). This approach demonstrated an improvement in the catalytic efficiency of the material, reaching a degradation percentage of 99.94% in 30 minutes in the presence of UV radiation compared to 96.50% in daylight, as illustrated in Fig. 6c. In order to determine the origin of this improvement, several other experiments were conducted. To this end, the exposure of 250 mL of IC solution to UV light under stirring in the absence of hydrogen peroxide and material (photolysis)

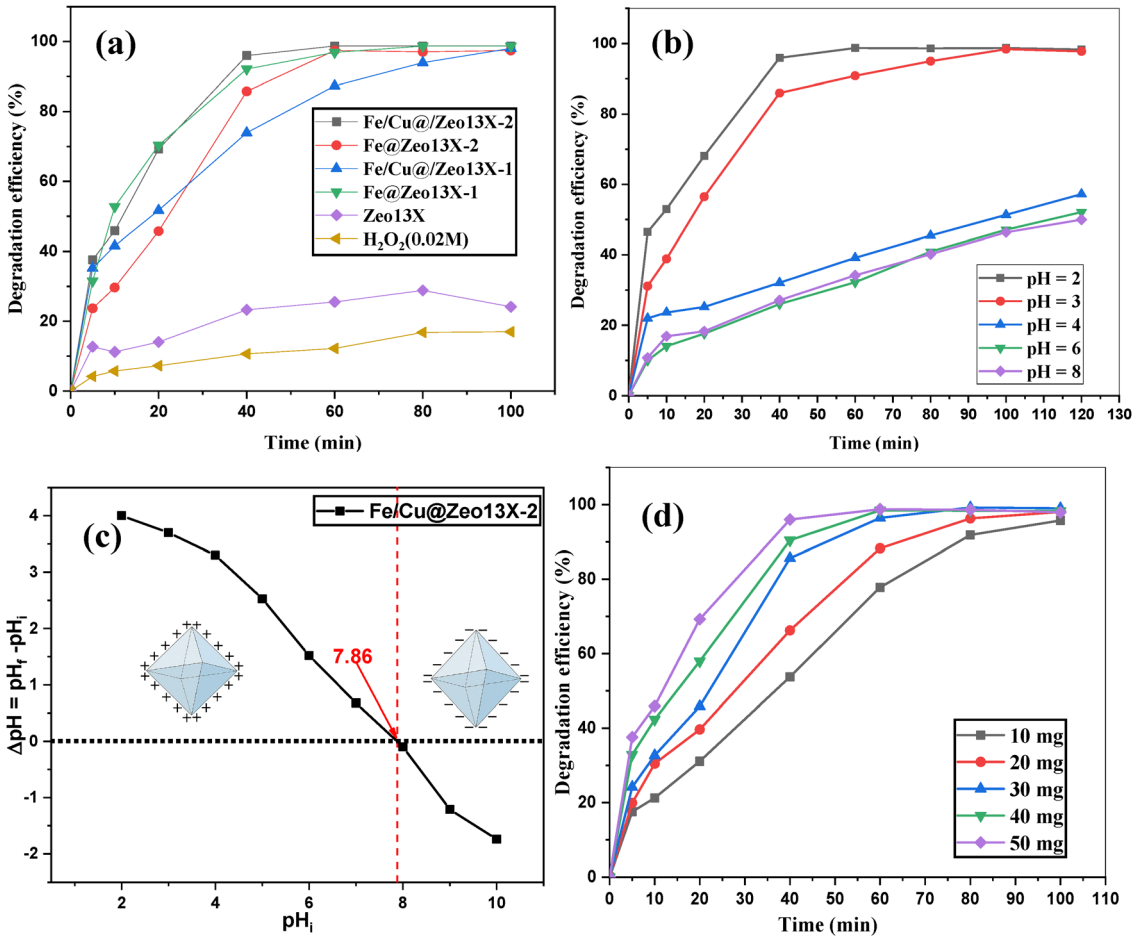

Fig. 5 Fenton-type degradation of IC: effect of post-synthetic treatment (a); effect of pH (b); zero charge point pH (c); effect of catalyst mass (d).

does not offer any degradation indicator. Maintaining the same experimental conditions, the application of 50 mg of catalyst to the elimination of IC, offers a percentage of elimination of 70.87% under UV irradiation (Fig. 6d). This considerably high percentage compared to that obtained in a daylight adsorption process (35.99%) highlights the capacity of the material to absorb light in the UV range. Thus, the improvement of the degradation of IC could be linked to the generation of superoxide radicals ($^{\bullet}O_2^-$), holes (h^+) or $^{\bullet}OH$ radicals resulting from the excitation of the valence electrons of Cu_2O and Fe_3O_4 nanoparticles by photons, in a purely photocatlytic process. For more precision, reactive species trapping tests were performed using several scavengers, including *n*-butanol for $^{\bullet}OH$, ammonium oxalate (AO) for h^+, and *p*-benzoquinone (*p*-b) for $^{\bullet}O_2^-$. For each experiment, 5 mL of solution of each of the above species at a concentration of 10 mM was added to the reaction mixture (250 mL of 50 mg L^{-1} IC solution, pH = 2, 50 mg of catalyst, 5 mL of 0.02 M H_2O_2) under UV irradiation. The results obtained are shown in Fig. 7a and b. It appears that the addition of *n*-butanol to the reaction medium causes a slight reduction in the percentage of elimination, suggesting a low contribution of $^{\bullet}OH$ radicals in the photocatalytic process studied.[75] On the other hand, the addition of *p*-b leads to a significant reduction in the percentage of elimination, highlighting the significant role of $^{\bullet}O_2^-$ radicals in the degradation process.[76,77] However, AO causes the greatest reduction in the elimination percentage. This observation suggests that h^+ are primarily responsible for the degradation of IC in the system studied.[48]

Given the presence of various inorganic ions in water contaminated with organic pollutants,[78] it is necessary to evaluate the effect of some of these ions on the degradation process in order to achieve more realistic conditions. To this end, the photo-Fenton degradation of IC by the Fe/Cu@Zeo13 catalyst was studied in the presence of different ions: Na^+, K^+, Mg^{2+}, Ca^{2+}, Ba^{2+}, Cl^-, CO_3^{2-}, $H_2PO_3^-$, and SO_4^{2-}. For each experiment, 0.1 g of metal salt containing one of these ions was added to the reaction mixture (250 mL of 50 mg L^{-1} IC solution, pH = 2, 50 mg of catalyst, 5 mL of 0.02 M H_2O_2) under UV irradiation, and the results obtained are shown in Fig. 7c–f. These results reveal that the presence of these ions causes a slight reduction in the percentage of IC dye removal, probably due to interference related to the adsorption of certain ions and the reactions that these ions have with certain reactive species, particularly holes and hydroxyl radicals.[78,79] This observation is consistent with certain reports in the literature, which have

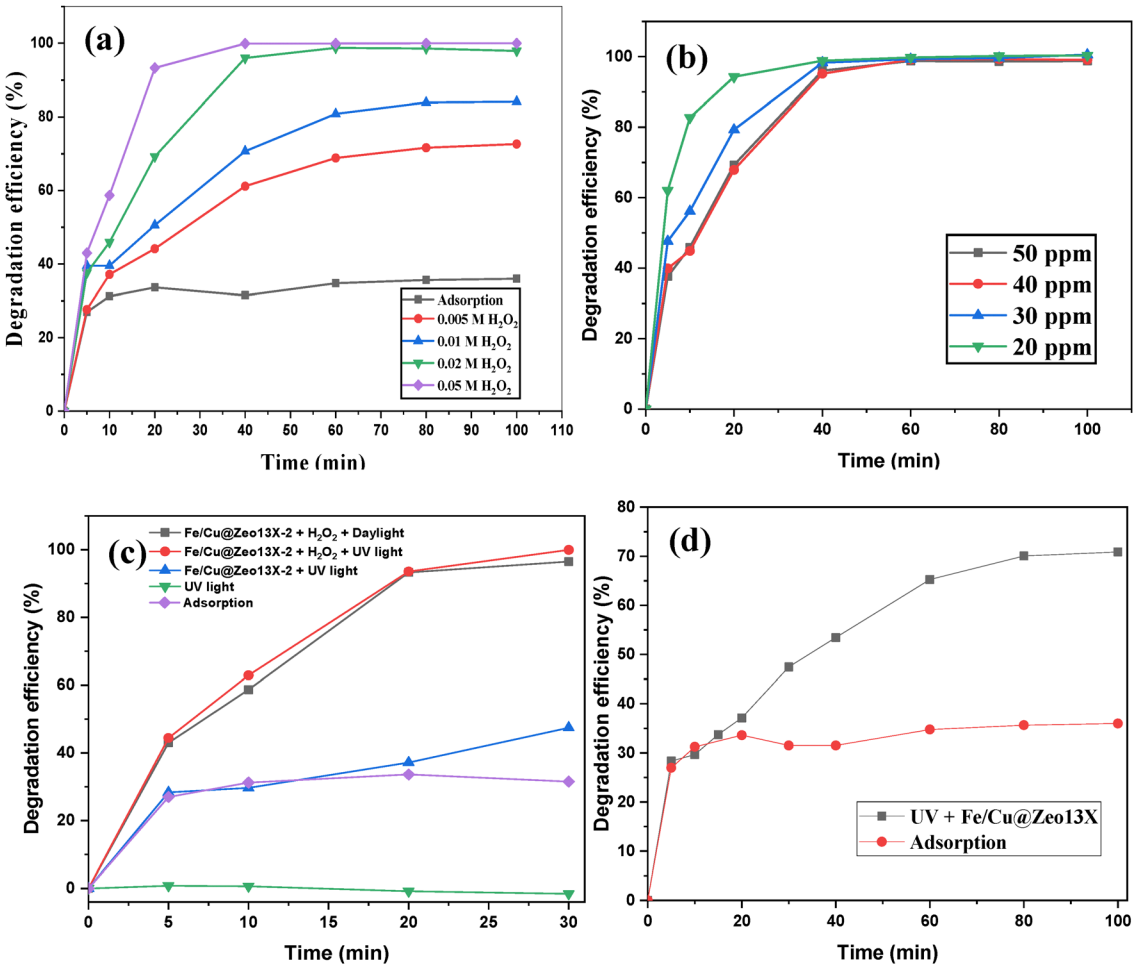

Fig. 6 Fenton-type degradation of IC: Effect of H_2O_2 concentration (a) effect of IC concentration (b); effect of radiation (60 W m^{-2}, λ_{max} = 368 nm) (c); photocatalytic properties of Fe/Cu@Zeo13X-2 (60 W m^{-2}, λ_{max} = 368 nm) (d).

revealed that inorganic ions are likely to inhibit the photodegradation of molecules such as bisphenol A, methyl orange, and carbamazepine.[78–80]

3.3. Application of Fe/Cu@Zeo13X-2 catalyst to optimize TC degradation

3.3.1. Validation and analysis of the model. Due to its exceptional catalytic and photocatalytic properties, the Fe/Cu@Zeo13X-2 catalyst was applied to the photo-Fenton degradation of TC, under the operating conditions defined in paragraph 2.5. In this context, a central composite design was used to evaluate the effects of variables during the degradation process. Thus, an experimental design of 27 experiments was implemented to determine the optimal conditions, and the results obtained are represented in Table 7. Based on these results, a quadratic model represented by eqn (14) was generated by the Design-Expert software to predict the evolution of TC degradation as a function of the variables used. The choice of the quadratic model was suggested by the software due to its coefficient of determination R^2 close to unity (0.975), and that of the R^2 adjusted (0.946) being close to R^2 as well as the value of the predicted R^2. The standard deviation for this model was 7.24, according to the data in Table 8, which represents the model summary statistics.

$$\%R = 69.007 + 2.41971A + 33.2505B + 4.64469C + 2.11039D - 3.06185AB + 1.25907AC + 0.354445AD - 1.07256BC + 0.222578BD + 2.02651CD - 10.3635A^2 - 24.4225B^2 + 8.10534C^2 + 2.62698D^2 \quad (14)$$

Eqn (14) suggests that the terms A, B, C, D, AC, AD, BD, CD, C^2 and D^2 exert a positive influence on the TC removal efficiency by Fe/Cu@Zeo13X-2, while the terms AB, BC, A^2 and B^2 have a negative impact. Furthermore, it is evident from this equation that the factor B, which represents the TC concentration, is the most significant factor. This observation is confirmed on the one hand by the perturbation diagram shown in Fig. 8a (diagnostic analysis) and on the other hand by the analysis of variance (ANOVA), which presents for this factor the lowest *p*-value (Table 9). In addition to the factor B, the terms C, A^2 and B^2 are significant, as indicated by the *p*-values lower than 0.05. These *p*-values are correlated with high *F*-

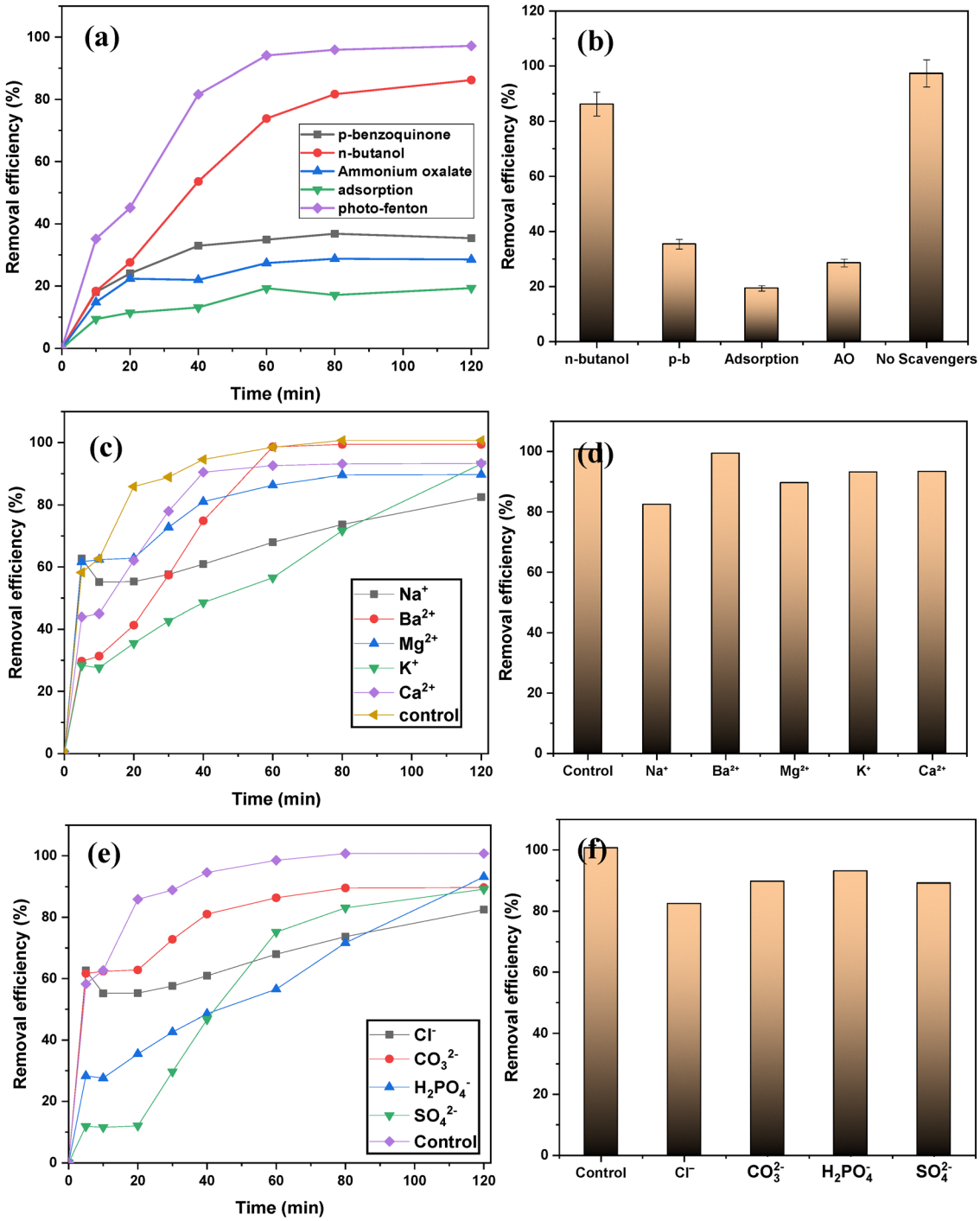

Fig. 7 Photo degradation of IC: (a) and (b) effect of scavengers on the degradation efficiency, (c) and (d) effect of cations on the degradation efficiency, (e) and (f) effect of anions on the degradation efficiency.

values. Furthermore, the low p-value of the model (<0.0001) and the F-value of 33.51 confirm the applicability of the model. The ability of this model to explore the experimental domain is further highlighted by the adequate precision value evaluated at 15.901 (greater than 4), which measures the signal-to-noise ratio and compares the range of the predicted value at the design points to the average prediction error.[81]

The diagnostic analysis of the model was also used to confirm its statistical robustness and its adequacy for prediction. These qualities were highlighted by the distribution curve of predicted values as a function of actual values (Fig. 8b), whose points follow a linear trend. The resulting residuals present a random character as illustrated by the residual plot as a function of experiments (Fig. 8c). The absence of apparent

Table 7 Experimental plan

Run	A: pH	B: TC concentration (mg L^{-1})	C: Mass (mg)	D: Time (min)	% R		
					Actual value	Predicted value	Residual
1	6	15	10	15	75.63	72.47	3.16
2	9	25	10	25	78.73	73.39	5.33
3	3	15	30	15	61.38	56.22	5.16
4	3	5	50	25	20.15	14.24	5.91
5	6	25	30	15	84.36	77.84	6.53
6	9	5	50	5	20.16	19.89	0.2693
7	6	15	50	15	77.23	81.76	−4.53
8	9	25	50	25	86.69	87.11	−0.4152
9	9	15	30	15	54.54	61.06	−6.52
10	6	15	30	15	72.15	69.01	3.15
11	6	15	30	15	72.42	69.01	3.41
12	3	5	10	5	3.84	2.26	1.58
13	3	25	50	25	79.21	85.16	−5.95
14	6	15	30	15	66.54	69.01	−2.47
15	6	15	30	25	66.81	73.74	−6.94
16	9	25	50	5	77.16	77.68	−0.5156
17	6	15	30	5	75.09	69.52	5.57
18	3	25	10	25	77.38	76.48	0.8979
19	9	5	10	5	15.12	9.99	5.13
20	6	5	30	15	3.44	11.33	−7.89
21	3	25	50	5	82.70	77.15	5.54
22	3	5	50	5	0.9597	7.12	−6.16
23	3	5	10	25	0.9597	1.27	−0.3103
24	9	5	50	25	34.27	28.43	5.84
25	9	25	10	5	67.32	72.07	−4.75
26	9	5	10	25	6.05	10.42	−4.38
27	3	25	10	5	69.91	76.58	−6.67

Table 8 Fit statistics

Source	Std. Dev.	R^2	Adjusted R^2	Predicted R^2
Linear	14.71	0.8114	0.7771	0.7377
2FI	16.76	0.8218	0.7104	0.4599
Quadratic	**7.24**	**0.9751**	**0.9460**	**0.8441**
Cubic	2.98	0.9986	0.9909	0.8975

structure of the residuals as a function of the initial TC concentration, catalyst mass, pH and time, illustrated by Fig. S1, confirms their independence from these factors. These results are in perfect consistency with the residual plot as a function of predicted values, represented in Fig. 8d. The latter reveals a random distribution of the residuals within the limits of ±4. Furthermore, the normal probability plot of the residuals (Fig. 8e) demonstrated a linear distribution of the points, confirming the absence of the need for transformation of the response variable, a conclusion corroborated by the Box-Cox plot (Fig. 8f) whose 95% confidence lambda was 1. Inspection of the leverage plot (Fig. 8g) indicated that all observations fell within the conventional range of 0 to 1, attesting that no data point exerted an excessive influence on the model fit. However, the Cook's distance analysis (Fig. 8h) identified experiment 27 as a potentially influential point, this observation also having a DFFITS value exceeding the threshold of acceptability. Nevertheless, the majority of quantitative indicators DFBETAS and DFFITS (Fig. 8i and j) remained within the admissible limits defined by the adjusted threshold, thus minimizing the impact of outlier observations on the overall validity and reliability of the model.[82] Consequently, the developed model is considered suitable for the prediction of the percentage of TC degradation with the Fe/Cu@Zeo13X-2 catalyst and for the determination of the optimal conditions.

3.3.2. Influence of different parameters on the degradation of TC by Fe/Cu@Zeo13X-2. The 3D and 2D representations of the response surfaces, which give the evolution of the percentage of degradation are shown in Fig. 9 and Fig. S2 respectively. These graphs clearly illustrate the significant effect of the TC concentration on removal efficiency. Indeed, graphs Fig. 9a, b and e reveal that an increase in the TC concentration from 5 to 25 mg L^{-1} leads to a significant increase in the efficiency. This trend is however modified when the pH and the catalyst mass increase. To this end, the antagonistic effect of the AB interaction on the efficiency is visible in graph Fig. 9e. The evolution of the efficiency as a function of the catalyst mass, when the latter increases from 10 to 50 mg, presents a rather unusual appearance according to graphs Fig. 9a, c and d. This is characterized by an initial decrease in the efficiency followed by an increase. The observed decrease could be explained by the increase in turbidity, which limits the penetration of UV light into the reaction mixture, thus reducing the photocatalytic activity of the catalyst.[74] However, the lack of light in the reaction medium can be overcome by a multiplication of active sites. This probably explains the increase in yield that follows as the mass continues to increase. Just like the mass, pH has an ambivalent effect on the removal efficiency (see Fig. 9d, e and f), when it increases from 3 to 9. An increase in pH first increases the yield to its maximum around pH = 6, before starting to decrease. This trend, regularly observed during the degradation of antibiotics, could be explained by the evolution of the charges on the surface

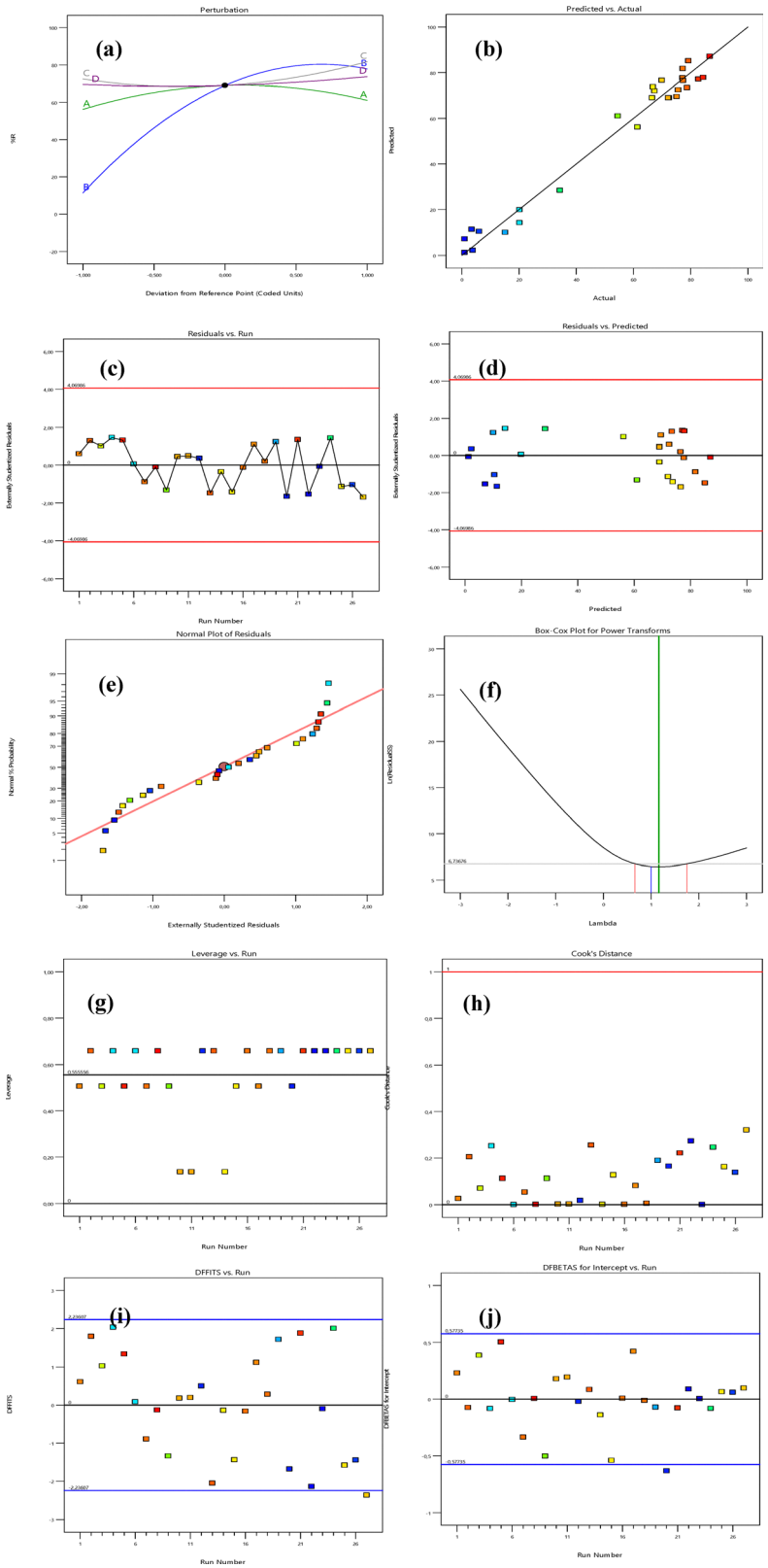

Fig. 8 Diagnostic analysis: (a) disturbance diagram; (b) predicted *vs.* actual; (c) residuals *vs.* run; (d) normal plot of residuals; (e) normal plot of residuals; (f) box-Cox plot for power transforms; (g) lifting *vs.* run; (h) cook's distance; (i) DFFITS *vs.* run; (j) DFBETAS *vs.* run.

of the catalyst and on the TC molecule as a function of the pH of the medium, as illustrated in Fig. 10a.[33,83] Indeed, the presence of three ionizable functional groups on the TC molecule gives it three values of pK_a (3.3, 7.7 et 9.7). Thus, this amphoteric molecule can

Table 9 Analysis of variance (ANOVA) of the model used

Std	Source	Sum of squares	Df	Mean square	*F*-Value	*p*-Value	
	Model	24 604.12	14	1757.44	33.51	< 0.0001	S
21	A-pH	105.39	1	105.39	2.01	0.1818	NS
12	B-TC concentration	19 900.74	1	19 900.74	379.41	< 0.0001	S
17	C-mass	388.32	1	388.32	7.40	0.0186	S
13	D-time	80.17	1	80.17	1.53	0.2400	NS
20	AB	150.00	1	150.00	2.86	0.1166	NS
6	AC	25.36	1	25.36	0.4836	0.5001	NS
22	AD	2.01	1	2.01	0.0383	0.8481	NS
16	BC	18.41	1	18.41	0.3509	0.5646	NS
18	Comics	0.7927	1	0.7927	0.0151	0.9042	NS
26	CD	65.71	1	65.71	1.25	0.2849	NS
25	A^2	276.18	1	276.18	5.27	0.0406	S
1	B^2	1533.75	1	1533.75	29.24	0.0002	S
15	C^2	168.93	1	168.93	3.22	0.0979	NS
27	D^2	17.75	1	17.75	0.3383	0.5716	NS
24	Residual	629.42	12	52.45			
8	Lack of fit	607.38	10	60.74	5.51	0.1633	NS
23	Pure error	22.04	2	11.02			
11	Total horn	25 233.55	26				

S: significant; NS: not significant

be found in several different forms in aqueous solution, including the cationic, Zwitterionic and anionic form (first monovalent to 7.7 < pH < 9.7 then divalent).[84] In this context, the positive charges of the cationic form of the TC molecule and of the surface of the Fe/Cu@Zeo13X-2 catalyst at pH < 3.3 are likely to generate electrostatic repulsions which lead to a reduction in favorable interactions. The same phenomenon can be observed at pH > 7.86, where both the TC molecule and the catalyst are negatively charged. Thus, TC is more favorable to degradation in its zwitterionic form where its negative charge can interact with the positive charges on the catalyst surface to promote its degradation.

The optimization of the TC degradation process by the Fe/Cu@Zeo13X catalyst using the response surface method made it possible to identify the optimal degradation conditions. It appears that a maximum removal percentage of 91.77% can be attained by combining the following conditions: pH = 6.76; TC concentration = 20.92 mg L^{-1}; mass = 48.66 and a time of 17.2 min. The experiment carried out under these conditions gives a percentage of 94.54%, which highlights the good fit between the model and experimental results. This yield exceeds that reported by numerous works on the degradation of both TC and IC using various heterogeneous catalysts as shown in Table 10.

3.4. Kinetic studies of IC and TC degradation by Fe/Cu@Zeo13X-2

The kinetic studies of IC and TC degradation were carried out by a linear fitting of the first (Fig. 11) and second (Fig. S3) order models to the experimental data. For this purpose, the second order model does not present a good fit, as illustrated by the low values of R^2 (Fig. S3). The study of the kinetics of TC degradation was carried out by evaluating the effect of the reaction time on the removal efficiency. Samples, taken at regular time intervals, were analyzed by UV-visible spectrophotometry to follow the evolution of the UV-visible profile of the solution. This evolution, illustrated in Fig. 10b, suggests the absence of production of impurities during the degradation and an almost total mineralization in 30 minutes. Furthermore, none of the kinetic models used seems to be truly suitable to describe the degradation of TC by the Fe/Cu@Zeo13X-2 catalyst (see Fig. S3c and Fig. 11a). In the case of IC, the modeling was done using the data obtained during the study of the influence of the initial concentration of this dye and H_2O_2. The results obtained reveal that the first-order model can be used to describe the degradation kinetics of IC at different concentrations of IC and H_2O_2, (except for $[H_2O_2]$ = 0.01 M et 0.05 M), according to the values of R^2 greater than 0.9. The rate constants and half-life times determined from this model are shown in Table 11. It follows logically that an increase in the initial concentration of IC between 20 and 50 mg L^{-1} leads to a reduction in the rate constant which goes from 0.087 to 0.066 min^{-1}. This reduction in the rate constant is correlated with an increase in the half-life time. The opposite trend is observed when the H_2O_2 concentration increases from 0.02 to 0.05 M, as illustrated by the change in the rate constant and half-life time from 0.066 to 0.137 min^{-1} and from 10.502 to 5.059 min respectively.

In order to simplify the understanding of the mechanism involved during the degradation of IC. The Langmuir–Hinshelwood (LH) model was associated with the first-order model, which showed a good fit under these conditions. This model, commonly used in heterogeneous catalysis, assumes that the adsorption of IC and H_2O_2 molecules constitutes the rate-limiting step in the degradation process.[89] In the absence of data on the evolution of the hydrogen peroxide concentration during degradation, our study was limited to the evaluation of the behavior of the dye molecules. The LH model makes it possible to establish a relationship between the initial concentration C_0 of the substrate and the oxidation rate r_0, according to eqn (15)–(19) below.[90,91]

$$r = -\frac{dC}{dt} = \frac{k_r k_s C}{1 + k_s C} \quad (15)$$

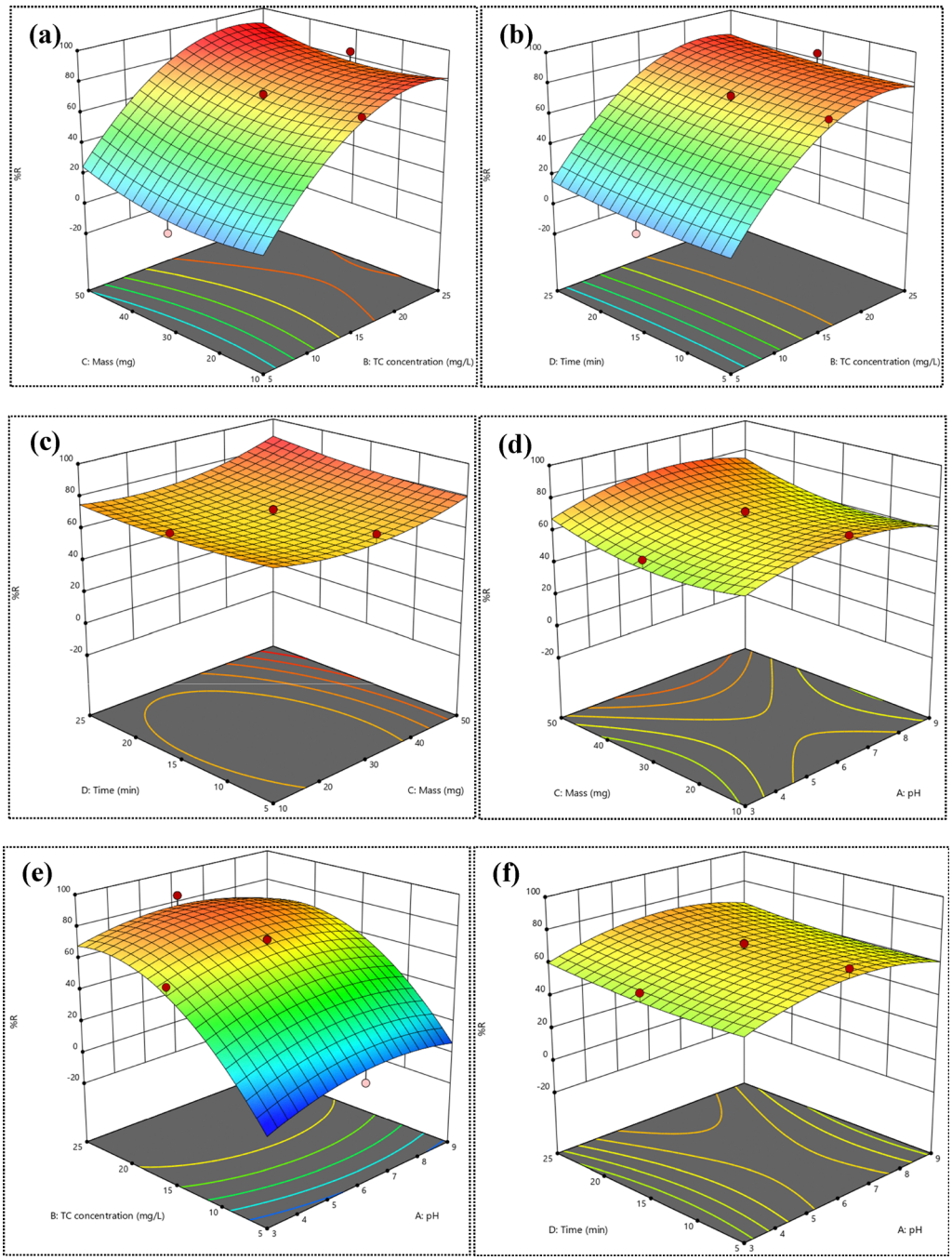

Fig. 9 Response surface curves of percentage of degradation (% R) against effects of TC concentration and catalyst mass (a), TC concentration and time (b), catalyst mass and time (c), pH and catalyst mass (d), pH and TC concentration (e), and pH and time (f) (18 W m^{-2}, λ = 365 nm).

where k_r, k_s and C represent respectively the rate constant of the reaction taking place at the surface of the catalyst in mg L^{-1} min^{-1}, the equilibrium constant of adsorption of LH in mg L^{-1} and the concentration of the dye IC in mg L^{-1}. The linear form of this equation is given by eqn (16). The integration of eqn (15) for $C \in [C_0;C]$ et $t \in [0;t]$, for $kC \ll 1$ leads to first-order kinetics given by relations (17) and (18), in which k_{app} is the apparent rate constant, given previously in Table 11. Under these conditions, eqn (16) can take the form of eqn (19). The latter can be used to determine the constants k_r and k_s, through the representation of the graph $1/k_{app}$ *vs.* C_0, where C_0 represents the initial concentration of dye.

$$\frac{1}{r} = \frac{1}{k_r} + \frac{1}{k_r k_s C} \quad (16)$$

$$r = k_{app} C \quad (17)$$

$$\ln\left(\frac{C_0}{C}\right) = k_{app} t \quad (18)$$

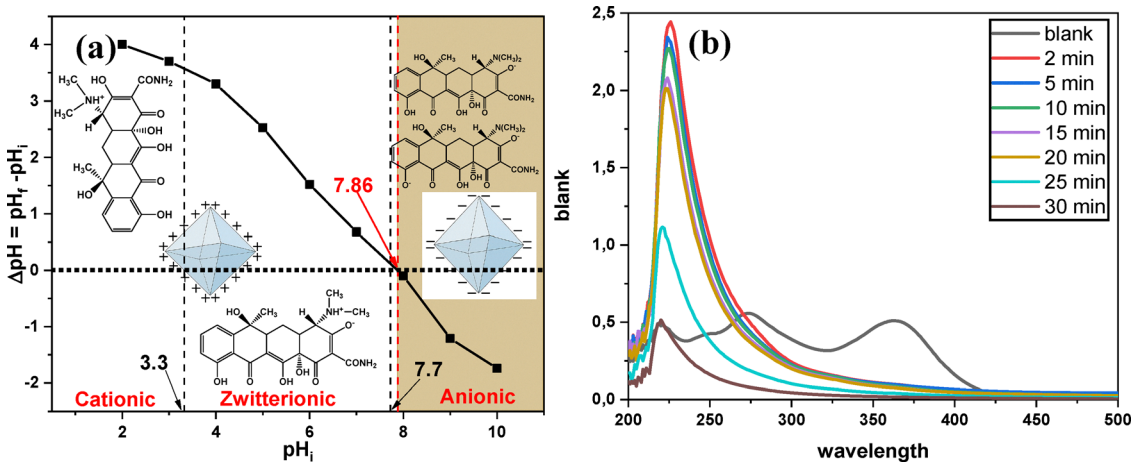

Fig. 10 Relation of catalyst surface charge and TC ionic forms as a function of pH (a); UV-visible profile of TC solutions during the degradation (b).

Table 10 Comparative table of Fe/Cu@Zeo13X-2 catalyst with previous works

Catalyst	Pollutant	pH	H_2O_2	Catalyst loading (g L^{-1})	Pollutant concentration (mg L^{-1})	Time (min)	Lighting	Elimination percentage (%)	Ref.
Ferromagnetic biochar	IC	3	5 mL; 4 M	3	100	240	—	99.97	49
Iron loaded graphitic Carbon	TC	4.3	1 mM	0.02	40	10	—	>83	85
$Fe_2V_4O_{13}$ nanoparticle	IC	4	0.3 mM	0.07	0.1 M	10	—	>90	86
Cerium-Doped MIL88-A/g-C_3N_4	TC	7	100 mg L^{-1}	0.5	50	100	Black	92.44	87
$FeNi_3/SiO_2/CuS$	TC	5	150 mg L^{-1}	0.005	10	200	UV	96	83
$FeNi_3/SiO_2$	TC	7	200 mg L^{-1}	0.1	20	180	—	92.3	88
Fe/Cu@Zeo13X-2	IC	2	5 mL; 0.05 M	0.2	50	60	Daylight	99.96	This study
Fe/Cu@Zeo13X-2	TC	6	5 mL; 0.5 M	~1	20.92	17.2	UV	94.54	This study

$$\frac{1}{k_{app}} = \frac{C_0}{k_r} + \frac{1}{k_r k_s} \quad (19)$$

The plot of C_0 *vs.* $1/k_{app}$ shown in Fig. 11d shows a linear trend with a coefficient of determination close to unity (R^2 = 0.9923). This observation reflects the good fit of the LH model to the experimental data, thus confirming the importance of adsorption in the degradation of IC. The resulting LH equilibrium constant is k_s = 0.0141 mg L^{-1} while the rate constant is k_r = 7.962 mg L^{-1} min^{-1}.

3.5. Mechanism of action of the Fe/Cu@Zeo13X-2 catalyst during the degradation reaction

According to the results of the kinetic studies, the most plausible mechanism of action of Fe/Cu@Zeo13X-2 for the degradation of the two pollutants studied begins with the adsorption of the latter in the company of H_2O_2. The latter reacts with the Fe^{2+} and Cu^+ metal species present on the surface of the catalysts to generate HO• radicals, which can in turn react with the IC and TC molecules adsorbed on the surface of the catalyst according to the mechanism described by Bopda *et al.*,[49] and Eltaweil *et al.*,[87] for IC and TC respectively, until mineralization which results in the formation of CO_2 and H_2O. The production of HO• radicals in this process is maintained by the continuous regeneration of Fe^{2+} species through the reaction between generated Fe^{3+} and Cu^+ (eqn (12)). The application of Fe/Cu@Zeo13X-2 to the photo-Fenton process leads to the formation of additional •OH radicals to which are added superoxide radicals ($^{\bullet}O_2^-$) originating respectively from the reactions of H_2O and O_2 with hole/electron pairs resulting from the excitation of the valence electrons of Cu_2O by photons, which move towards the conduction band of Cu_2O and Fe_3O_4.[28,31] The results of active species trapping tests (Section 3.2.3) established that the photodegradation of IC is mainly attributed to h^+ and $^{\bullet}O_2^-$ radicals. Conversely, •OH radicals show only a small contribution to the process. This mechanism, involving h^+ and $^{\bullet}O_2^-$ as the main oxidants, is undoubtedly the same as that governing the photodegradation of the TC molecule. Fig. 12 illustrates the mechanism of action of the catalyst.

3.6. Stability of the Fe/Cu@Zeo13X-2 catalyst

The study of catalyst reusability is an essential process to evaluate their stability and applicability on an industrial scale.[92] In this study, after each experiment, the materials were recovered by centrifugation and then washed several times with distilled water and dried in an oven before being applied in a new degradation cycle. The successive experiments carried out under the same conditions show a slight decrease in the degradation percentage from 94.54 to 76.01% after six TC

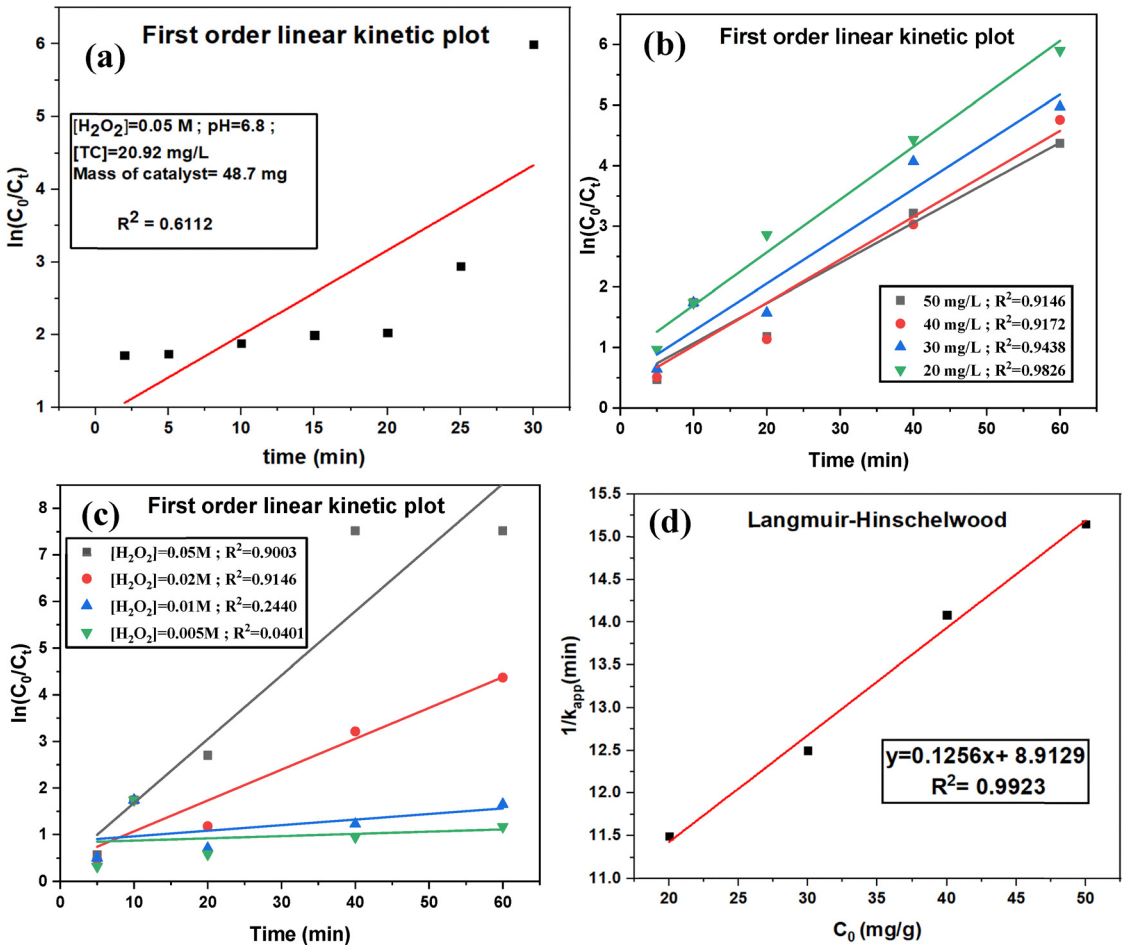

Fig. 11 First-order kinetics associated with TC (a) and IC (b) degradation; second-order (c) and LH (d) associated with IC degradation.

Table 11 First-order kinetic parameters for IC degradation by Fe/Cu@Zeo13X-2

	IC concentration (mg L^{-1})			
Settings	50	40	30	20
R^2	0.9146	0.9172	0.9438	0.9826
k (min^{-1})	0.066	0.071	0.080	0.087
$t_{1/2}$ (min)	10.502	9.763	8.664	7.967
	$[H_2O_2]$ (M)			
Settings	0.05	0.02	0.01	0.005
R^2	0.9003	0.9146	0.2440	0.0401
k (min^{-1})	0.137	0.066	0.0112	0.005
$t_{1/2}$ (min)	5.059	10.502	61.888	138.629

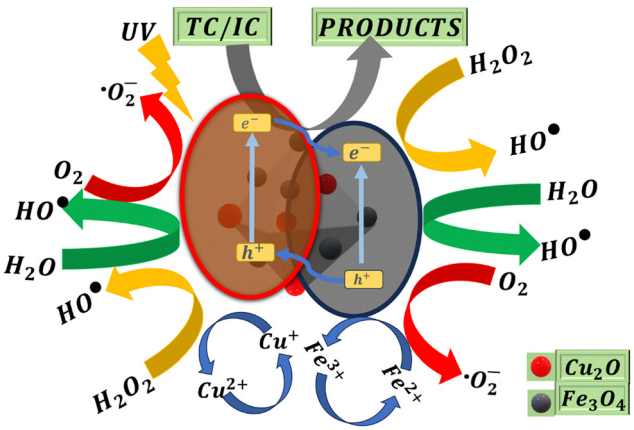

Fig. 12 Mechanism of action of Fe/Cu@Zeo13X-2 during TC and IC photo-Fenton degradation.

degradation cycles and from 98.74 to 87.78% after five IC degradation cycles, as illustrated in Fig. 13a and b). These results suggest that the Fe/Cu@Zeo13X-2 catalyst can be used for several cycles, particularly for the removal of IC. The high performance observed in the first cycle can be attributed to the availability of active sites on the catalyst surface. The gradual decline in efficiency observed from the second cycle onwards may be due to several factors, including the gradual diffusion of the catalyst during the recovery process, and the potential blocking of active sites by TC and IC molecules.[76,93] In addition, a gradual alteration in the structure of the material is likely to explain the reduction in its efficiency. This latter hypothesis is supported by the XRD pattern of the material after IC

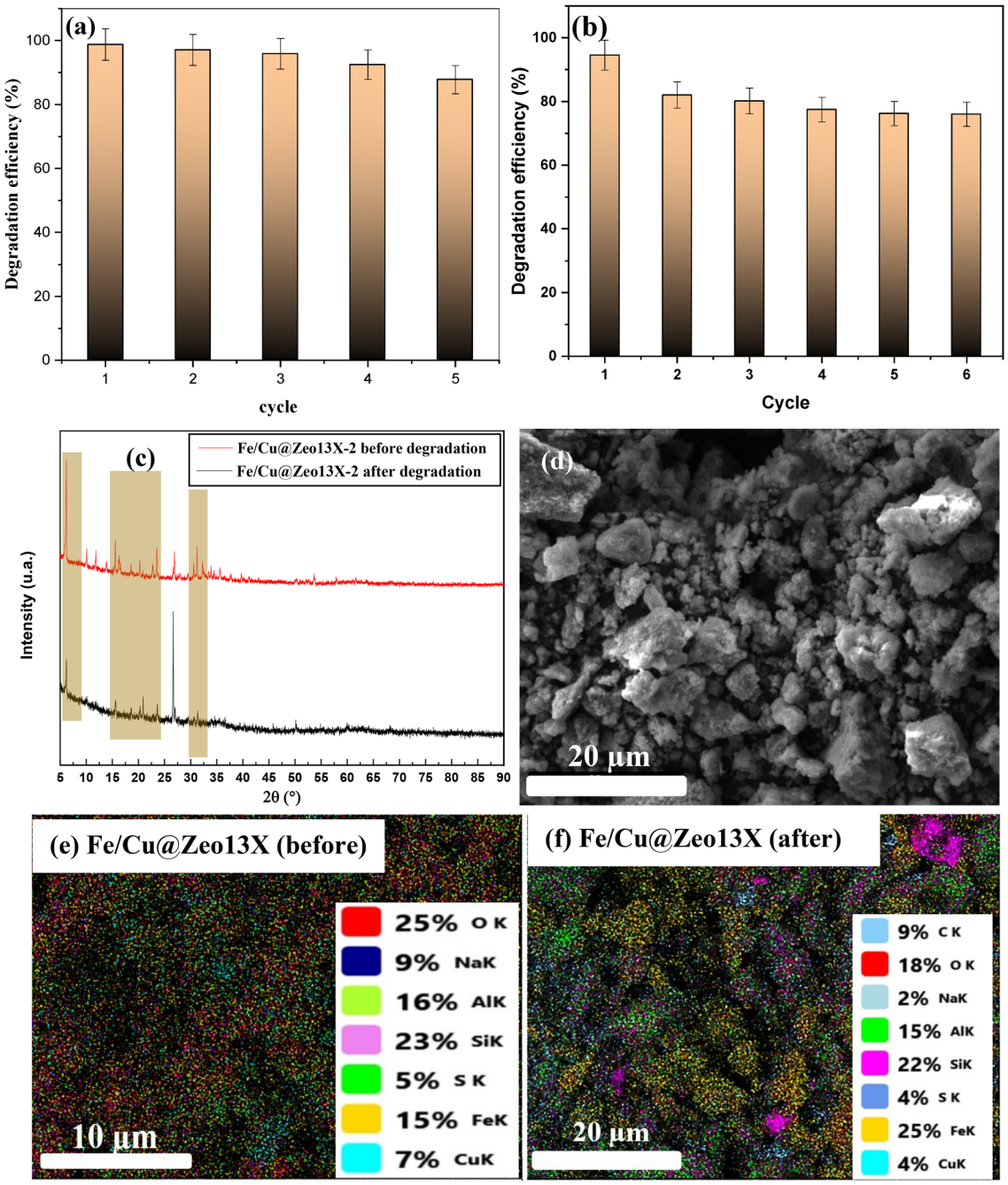

Fig. 13 Stability of Fe/Cu@Zeo13X-2 catalyst on the IC (a) and TC (b) degradation, XRD (c), SEM (d) and EDX-mapping (e) and (f) analyses of Fe/Cu@Zeo13X after degradation.

degradation (Fig. 13c), which shows a significant reduction in the diffraction lines of Fe/Cu@Zeo13X-2 and the appearance of an intense line at 26.52°. This transformation of the XRD pattern, to which is added a slight modification of the morphology of the samples given by SEM (Fig. 13d), could be linked to the adsorption of IC and H_2O_2 molecules on the surface of the catalyst which hinders the diffusion of X-rays. This is materialized by the appearance of the element carbon on the surface of Fe/Cu@Zeo13X-2, as illustrated by the images obtained by EDX mapping (Fig. 13e and f). However, the presence of areas with very high Si content on the material could indicate a release of Fe and Cu species in solution. These results contribute to positioning the Fe/Cu@Zeo13X-2 catalyst as an alternative for the removal of IC dye and TC antibiotic from aqueous solutions.

4. Conclusion

Heterogeneous catalysts, Fe@Zeo13X and Fe/Cu@Zeo13X, were synthesized from a combination of zeolite X and magnetite to

eliminate IC dye and the TC antibiotic from an aqueous solution. These syntheses were performed using a hydrothermal-assisted precipitation/co-precipitation method. The zeolite modification process was confirmed successful through various physicochemical analyses. However, these analyses revealed significant changes in the zeolite's structural, morphological, optical, and electrochemical properties. The catalytic properties of the materials were evaluated in degradation of IC. It appears that the Fe/Cu@Zeo13X material has the best catalytic activity, with a maximum removal percentage of 99.96% under optimal conditions. The study of the effect of UV radiation has highlighted the photocatalytic properties of this material, which has motivated its application to the optimization of the degradation of TC in aqueous solution. The results obtained give a maximum degradation efficiency of 94.54% under optimal conditions. Kinetic studies have revealed that the first-order model is the most appropriate to describe the degradation kinetics of IC in aqueous solution. The application of the Langmuir–Hinshelwood model made it possible to highlight the preponderant role of adsorption during the degradation of pollutants. However, none of the models used seems appropriate to describe the degradation kinetics of TC on Fe/Cu@Zeo13X. The study of the catalyst's reusability highlighted its ability to be used multiple times in each degradation process studied, thus confirming its stability. This stability was further confirmed by the characterization of the material after use. This study is part of the search for effective and less expensive solutions for the elimination of organic pollutants in aqueous solution.

Author contributions

Frank Dorinel Solefack Feudjio: writing – original draft, visualization, validation, resources, methodology, investigation, formal analysis, data curation, conceptualization. Christian Brice Dantio Nguela: visualization, resources, methodology, investigation, formal analysis. Georges Teikam Kenda and Donald Raoul Tchuifon Tchuifon: visualization, validation, methodology, investigation, formal analysis, data curation. Roussin Lontio Fomekong: visualization, validation, methodology, investigation, formal analysis. Julius Nsami Ndi, Horace Manga Ngomo and Rhaman Abdoul Ntieche: validation, supervision, writing – review & editing, resources, funding acquisition, project administration. Cyrille Ghislain Fotsop: validation, formal analysis, data curation, writing – review & editing.

Conflicts of interest

The authors declare no conflict of interest.

Data availability

Data available on request.

The data supporting this article have been included as part of the supplementary information (SI). Supplementary information is available. See https://doi.org/10.1039/d5ma01113b.

Acknowledgements

The authors thank the Applied Physical and Analytical Chemistry Laboratory (APACL), Faculty of Science, University of Yaoundé I, Cameroon for the logistic and materials.

References

1 H. S. Sherry, Ion Exchange, in *Handbook of Zeolite Science and Technology*, CRC Press, 2003, pp. 1271–1253.
2 S. A. Johnson, E. S. Brigham and P. J. Ollivier, *et al.*, Effect of Micropore Topology on the Structure and Properties of Zeolite Polymer Replicas, *Chem. Mater.*, 1997, **9**(11), 2448–2458, DOI: 10.1021/cm9703278.
3 M. Yoldi, E. G. Fuentes-Ordoñez and S. A. Korili, *et al.*, Zeolite synthesis from industrial wastes, *Microporous Mesoporous Mater.*, 2019, **287**, 183–191, DOI: 10.1016/j.micromeso.2019.06.009.
4 K. L. T. Nguena, C. G. Fotsop and S. B. L. Ngomade, *et al.*, Mathematical modeling approach for the green synthesis of high-performance nanoporous zeolites Na-X optimized for water vapor sorption, *Mater. Today Commun.*, 2023, **37**, 107406, DOI: 10.1016/j.mtcomm.2023.107406.
5 C. G. Fotsop, A. Lieb and F. Scheffler, Insights into the synergistic effects of ZnO/MgO and Zn/Mg-modified porous zeolite as core-satellite materials for tuning water vapor sorption properties, *Appl. Surf. Sci. Adv.*, 2025, **30**, 100855, DOI: 10.1016/j.apsadv.2025.100855.
6 C. G. Fotsop, A. Lieb and F. Scheffler, Tailoring the water vapor adsorption properties by thermal performance analysis of post-synthetically ion-exchanged LTA zeolite derived from Cameroonian kaolin, *J. Ind. Eng. Chem.*, 2025, DOI: 10.1016/j.jiec.2025.08.017.
7 F. D. S. Feudjio, C. G. Fotsop and D. R. T. Tchuifon, *et al.*, Tunable water vapor adsorption properties on ion exchange microporous zeolite Na-X derived from natural kaolin, *Inorg. Chem. Commun.*, 2025, **177**, 114379, DOI: 10.1016/j.inoche.2025.114379.
8 T. Feze Fanle, G. Teikam Kenda and D. R. Tchuifon Tchuifon, *et al.*, Design and characterisation of activated magnetic zeolite 4A from naturally occurring kaolin clay of Cameroonian origin for optimised dye removal by Fenton-like degradation, *Int. J. Environ. Anal. Chem.*, 2024, 1–29, DOI: 10.1080/03067319.2024.2389417.
9 R. U. N. Foko, C. G. Fotsop and D. R. T. Tchuifon, *et al.*, Green synthesis of magnetic type Zeolites 4A as catalyst for the elimination of quinoline yellow by the Fenton process: Optimization and kinetic investigation, *Hybrid Adv.*, 2025, **9**, 100401, DOI: 10.1016/j.hybadv.2025.100401.
10 S. B. L. Ngomade, C. G. Fotsop and A. K. Bhonsle, *et al.*, Pilot-scale optimization of enhanced biodiesel production

from high FFA Podocarpus falcatus oil via simultaneous esterification and transesterification assisted by zirconia-supported ZSM-5, *Chem. Eng. Res. Des.*, 2024, **209**, 52–66, DOI: 10.1016/j.cherd.2024.07.031.

11 P. L. Tran-Nguyen, K. Ly and S. P. Santoso, *et al.*, Iron oxides/zeolite X composite derived from rice husk ash: fabrication and physicochemical properties for superior heterogeneous Fenton-like oxidation of crystal violet, *J. Chem. Technol. Biotechnol.*, 2025, **100**(6), 1222–1237, DOI: 10.1002/jctb.7857.

12 C. G. Fotsop, A. Lieb and F. Scheffler, Highly efficient removal and separation of Sr^{2+}, Co^{2+}, In^{3+} and Ni^{2+} in single and mixed ion systems on low-cost Zeolite, and its stability analysis: DFT and experimental investigations, *Chem. Eng. J. Adv.*, 2026, **25**, 100986, DOI: 10.1016/j.ceja.2025.100986.

13 A. Rathi, S. Basu and S. Barman, Structural framework effect of various CeO2-loaded zeolites on the adsorptive removal of fipronil, *J. Environ. Chem. Eng.*, 2021, **9**(2), 105167, DOI: 10.1016/j.jece.2021.105167.

14 J. Rivera-Utrilla, M. V. López-Ramón and M. Sánchez-Polo, *et al.*, Characteristics and Behavior of Different Catalysts Used for Water Decontamination in Photooxidation and Ozonation Processes, *Catalysts*, 2020, **10**(12), 1485, DOI: 10.3390/catal10121485.

15 T. Yarnazari, B. Maleki and M. Mansouri, *et al.*, Zeolite 13X incorporated with Zn-Ce oxide nanocatalyst for removal of Reactive Red 120 dye: RSM-based approach, *Environ. Monit. Assess.*, 2024, **196**(4), 344, DOI: 10.1007/s10661-024-12505-5.

16 M. Zhang and X. Wang, Preparation of a Gangue-Based X-type Zeolite Molecular Sieve as a Multiphase Fenton Catalyst and Its Catalytic Performance, *ACS Omega*, 2021, **6**(28), 18414–18425, DOI: 10.1021/acsomega.1c02469.

17 J. J. Pignatello, Dark and photoassisted iron(3+)-catalyzed degradation of chlorophenoxy herbicides by hydrogen peroxide, *Environ. Sci. Technol.*, 1992, **26**(5), 944–951, DOI: 10.1021/es00029a012.

18 F. Zaviska, P. Drogui and G. Mercier, *et al.*, Procédés d'oxydation avancée dans le traitement des eaux et des effluents industriels: Application à la dégradation des polluants réfractaires, *Rev. Sci. Eau*, 2009, **22**(4), 535–564, DOI: 10.7202/038330ar.

19 F. Wang, D. W. Smith and M. G. El-Din, Application of advanced oxidation methods for landfill leachate treatment – A review, *J. Environ. Eng. Sci.*, 2003, **2**(6), 413–427, DOI: 10.1139/s03-058.

20 B. G. H. Briton, L. Duclaux and Y. Richardson, *et al.*, Effectiveness of the dispersion of iron nanoparticles within micropores and mesopores of activated carbon for Rhodamine B removal in wastewater by the heterogeneous Fenton process, *Appl. Water Sci.*, 2019, **9**(7), 166, DOI: 10.1007/s13201-019-1047-0.

21 W. Ma, K. Wang and S. Pan, *et al.*, Iron-Exchanged Zeolite Micromotors for Enhanced Degradation of Organic Pollutants, *Langmuir*, 2020, **36**(25), 6924–6929, DOI: 10.1021/acs.langmuir.9b02137.

22 S. Komtchou, A. Dirany and P. Drogui, *et al.*, Application des procédés d'oxydation avancée pour le traitement des eaux contaminées par les pesticides – revue de littérature, *Rev. Sci. Eau*, 2017, **29**(3), 231–262, DOI: 10.7202/1038926ar.

23 H. G. Quynh, N. A. Kiet and H. V. Thanh, *et al.*, Removal of aqueous organic pollutant by photo-Fenton process using low-cost Fe_3O_4/zeolite A, *IOP Conf. Ser.: Earth Environ. Sci.*, 2021, **947**(1), 012013, DOI: 10.1088/1755-1315/947/1/012013.

24 G. T. Kenda, P. A. N. Kouteu and D. R. T. Tchuifon, *et al.*, Green synthesis of magnetic biochars derived from bio-based orange peel materials as sustainable heterogeneous catalytic supports for the Fenton process, *Arabian J. Chem.*, 2024, **17**(2), 105502, DOI: 10.1016/j.arabjc.2023.105502.

25 D. R. Tchuifon Tchuifon, C. G. Fotsop and S. G. M. Mafo, *et al.*, Unveiling the photocatalytic activity of Cu/Fe2O3@gC3N4 nanosheet as an efficient Fenton-like catalyst for reactive blue 19 removal: Optimization and kinetics studies, *Hybrid Adv.*, 2025, **9**, 100424, DOI: 10.1016/j.hybadv.2025.100424.

26 J. Tang and J. Wang, MOF-derived three-dimensional flower-like FeCu@C composite as an efficient Fenton-like catalyst for sulfamethazine degradation, *Chem. Eng. J.*, 2019, **375**, 122007, DOI: 10.1016/j.cej.2019.122007.

27 F.-X. Wang, Z.-W. Zhang and F. Wang, *et al.*, Fe-Cu bimetal metal-organic framework for efficient decontamination via Fenton-like process: Synthesis, performance and mechanism, *J. Colloid Interface Sci.*, 2023, **649**, 384–393, DOI: 10.1016/j.jcis.2023.06.083.

28 J. Wang, L. Zhang and H. Zhang, *et al.*, Magnetically recyclable spherical Cu_2O@Fe_3O_4 S-scheme heterojunction for efficient tetracycline removal *via* visible light-activated peroxydisulfate, *RSC Adv.*, 2024, **14**(34), 24413–24423, DOI: 10.1039/D4RA04174G.

29 S. Li, R. Li and K. Dong, *et al.*, Self-floating $Bi_4O_5Br_2$/P-doped C_3N_4/carbon fiber cloth with S-scheme heterostructure for boosted photocatalytic removal of emerging organic contaminants, *Chin. J. Catal.*, 2025, **76**, 37–49, DOI: 10.1016/S1872-2067(25)64780-2.

30 S. Li, Y. Zhao and X. Zhang, *et al.*, Floatable S-scheme $Bi_4O_5Br_2$/C_3N_4/Carbon Fiber Cloth with Robust Internal Electric Field for Efficient Photocatalytic Antibiotic Decontamination, *Adv. Fiber Mater.*, 2025, **7**(6), 2032–2047, DOI: 10.1007/s42765-025-00601-1.

31 K. Wang, M. Xu and Z. Fang, *et al.*, Enhanced photocatalytic activity of magnetically recyclable spherical Fe_3O_4/Cu_2O S-scheme heterojunction, *Environ. Technol.*, 2024, **45**(20), 3986–4002, DOI: 10.1080/09593330.2023.2238131.

32 S. Li, X. Wang and B. Xue, *et al.*, Flower-like Ag/Ag2O/Bi12O17Cl2 heterojunction for photocatalytic removal of antibiotics: Synergetic effect of plasmonic effect and p–n heterojunction, *J. Mater. Sci. Technol.*, 2026, **246**, 237–246, DOI: 10.1016/j.jmst.2024.12.088.

33 X. Liang, L. Li and Y. Wu, *et al.*, Cu-doped Fe3O4 coupled to MIL-101(Fe) for the preparation of composites with enhanced photo-Fenton degradation of tetracycline hydrochloride, *J. Water Process Eng.*, 2025, **73**, 107698, DOI: 10.1016/j.jwpe.2025.107698.

34 I. Chopra and M. Roberts, Tetracycline Antibiotics: Mode of Action, Applications, Molecular Biology, and Epidemiology

of Bacterial Resistance, *Microbiol. Mol. Biol. Rev.*, 2001, **65**(2), 232–260, DOI: 10.1128/MMBR.65.2.232-260.2001.

35 M. L. Nelson and S. B. Levy, The history of the tetracyclines, *Ann. N. Y. Acad. Sci.*, 2011, **1241**(1), 17–32, DOI: 10.1111/j.1749-6632.2011.06354.x.

36 E. S. Allen and W. E. Brown, Hepatic toxicity of tetracycline in pregnancy, *Am. J. Obstet. Gynecol.*, 1966, **95**(1), 12–18, DOI: 10.1016/0002-9378(66)90623-5.

37 C. Glenn and S. R. Feldman, Tetracycline-induced hepatotoxicity, *Dermatol. Online J.*, 2011, **17**(12), DOI: 10.5070/D31DS9V5Z0.

38 D. Xu, Y. Xiao and H. Pan, *et al.*, Toxic effects of tetracycline and its degradation products on freshwater green algae, *Ecotoxicol. Environ. Saf.*, 2019, **174**, 43–47, DOI: 10.1016/j.ecoenv.2019.02.063.

39 Y. Dai, M. Liu and J. Li, *et al.*, A review on pollution situation and treatment methods of tetracycline in groundwater, *Sep. Sci. Technol.*, 2020, **55**(5), 1005–1021, DOI: 10.1080/01496395.2019.1577445.

40 Y. Amangelsin, Y. Semenova and M. Dadar, *et al.*, The Impact of Tetracycline Pollution on the Aquatic Environment and Removal Strategies, *Antibiotics*, 2023, **12**(3), 440, DOI: 10.3390/antibiotics12030440.

41 C. Wang, S. Wang and J. Zhang, *et al.*, The Biodegradation of Indigo Carmine by Bacillus safensis HL3 Spore and Toxicity Analysis of the Degradation Products, *Molecules*, 2022, **27**(23), 8539, DOI: 10.3390/molecules27238539.

42 M.-E. Ristea and O. Zarnescu, Indigo Carmine: Between Necessity and Concern, *J. Xenobiot.*, 2023, **13**(3), 509–528, DOI: 10.3390/jox13030033.

43 M.-E. Ristea and O. Zarnescu, Effects of Indigo Carmine on Growth, Cell Division, and Morphology of Allium cepa L. Root Tip, *Toxics*, 2024, **12**(3), 194, DOI: 10.3390/toxics12030194.

44 T. B. Zanoni, A. A. Cardoso and M. V. B. Zanoni, *et al.*, Exploratory study on sequestration of some essential metals by indigo carmine food dye, *Braz. J. Pharm. Sci.*, 2010, **46**(4), 723–730, DOI: 10.1590/S1984-82502010000400014.

45 M. De Keijzer, M. R. Van Bommel and R. H. Keijzer, *et al.*, Indigo carmine: Understanding a problematic blue dye, *Stud. Conserv.*, 2012, **57**(sup1), S87–S95, DOI: 10.1179/2047058412Y.0000000058.

46 B. Lellis, C. Z. Fávaro-Polonio and J. A. Pamphile, *et al.*, Effects of textile dyes on health and the environment and bioremediation potential of living organisms, *Biotechnol. Res. Innov.*, 2019, **3**(2), 275–290, DOI: 10.1016/j.biori.2019.09.001.

47 S. Muzammal, A. Ahmad and S. Atta, *et al.*, Sustainable synthesis of Nd_2O_3 nanoparticles for photocatalytic degradation of tetracycline in aqueous media, *Mater. Adv.*, 2025, **6**(21), 8011–8022, DOI: 10.1039/D5MA00615E.

48 S. A. Benedoue, J. N. Ndi and M. Ge, *et al.*, Controllable Acid Activation of Sulfur-Doped Carbon Nitride Enables Enhancement in Photocatalytic Indigo Carmine Degradation Performance, *ACS Sustainable Chem. Eng.*, 2024, **12**(45), 16809–16816, DOI: 10.1021/acssuschemeng.4c08021.

49 A. Bopda, S. G. M. Mafo and J. N. Ndongmo, *et al.*, Ferromagnetic Biochar Prepared from Hydrothermally Modified Calcined Mango Seeds for Fenton-like Degradation of Indigo Carmine, *C*, 2022, **8**(4), 81, DOI: 10.3390/c8040081.

50 W. Zou, L. Liu and L. Zhang, *et al.*, Crystal-plane effects on surface and catalytic properties of Cu_2O nanocrystals for NO reduction by CO, *Appl. Catal., A*, 2015, **505**, 334–343, DOI: 10.1016/j.apcata.2015.08.021.

51 P. Lorkit, M. Panapoy and B. Ksapabutr, Iron Oxide-based Supercapacitor from Ferratrane Precursor via Sol–gel-Hydrothermal Process, *Energy Procedia*, 2014, **56**, 466–473, DOI: 10.1016/j.egypro.2014.07.180.

52 F. Thibault-Starzyk, Introduction a l'etude Des Zéolithes Par Spectroscopie Infrarouge, in *Matériaux Micro et Mésoporeux*, EDP Sciences, Les Ulis, 2004, pp. 51–90, DOI: 10.1051/978-2-7598-0242-5.c004.

53 C. G. Fotsop, A. Lieb and F. Scheffler, Cameroonian natural clay derived Linde type LTA zeolite: demystifying and understanding the impact of the synthesis process on adsorption efficiency, *Mater. Adv.*, 2025, DOI: 10.1039/D5MA00915D.

54 L. Nalbandian, E. Patrikiadou and V. Zaspalis, *et al.*, Magnetic Nanoparticles in Medical Diagnostic Applications: Synthesis, Characterization and Proteins Conjugation, *CNANO*, 2016, **12**(4), 455–468, DOI: 10.2174/1573413712666151210230002.

55 S. Jadhav, S. Gaikwad and M. Nimse, *et al.*, Copper Oxide Nanoparticles: Synthesis, Characterization and Their Antibacterial Activity, *J. Clust. Sci.*, 2011, **22**(2), 121–129, DOI: 10.1007/s10876-011-0349-7.

56 J. Zhen, S. Zhang and X. Zhuang, *et al.*, Sulfate radicals based heterogeneous peroxymonosulfate system catalyzed by CuO-Fe_3O_4-Biochar nanocomposite for bisphenol A degradation, *J. Water Process Eng.*, 2021, **41**, 102078, DOI: 10.1016/j.jwpe.2021.102078.

57 S. Torres-Arellano, E. Luevano-Hipolito and M. G. Fabela-Cedillo, *et al.*, Optimized CO2 photoreduction using cuprous oxide (Cu_2O) nanoparticles synthesized using Psidium guajava extract, *Energy Ecol. Environ.*, 2025, **10**(1), 66–78, DOI: 10.1007/s40974-024-00331-x.

58 H. Gallard, J. De Laat and B. Legube, Étude comparative de la vitesse de décomposition de H_2O_2 et de l'atrazine par les systèmes Fe(III)/H_2O_2, Cu(II)/H_2O_2 et Fe(III)/Cu(II)/H_2O_2, *Rev. Sci. Eau*, 1999, **12**(4), 713–728, DOI: 10.7202/705374ar.

59 S. Li, C. You and K. Rong, *et al.*, Chemically bonded Mn0.5Cd0.5S/BiOBr S-scheme photocatalyst with rich oxygen vacancies for improved photocatalytic decontamination performance, *Adv. Powder Mater.*, 2024, **3**(3), 100183, DOI: 10.1016/j.apmate.2024.100183.

60 C. You, X. Zhang and Y. Zhao, *et al.*, Plasmonic effect augmented S-scheme mechanism in Ag/Ag_2O/C_3N_5 photocatalyst enables efficient photocatalytic degradation of antibiotics, *J. Mater. Sci. Technol.*, 2026, **242**, 64–74, DOI: 10.1016/j.jmst.2025.05.002.

61 G. T. Kenda, C. G. Fotsop and D. R. T. Tchuifon, *et al.*, Building TiO_2-doped magnetic biochars from Citrus sinensis peels as low-cost materials for improved dye degradation

using a mathematical approach, *Appl. Surf. Sci. Adv.*, 2024, **19**, 100554, DOI: 10.1016/j.apsadv.2023.100554.

62 G. K. R. Senadeera, C. A. Thotawatthage and M. A. K. L. Dissanayake, Efficiency enhancement in Dye Sensitized Solar Cells by light scattering in photoanode with TiO_2 nanotubes, *J. Phys: Conf. Ser.*, 2020, **1552**(1), 012002, DOI: 10.1088/1742-6596/1552/1/012002.

63 S. Srinivasa Rao, V. V. M. Gopi Chandu and S.-K. Kim, *et al.*, Cobalt sulfide thin film as an efficient counter electrode for dye-sensitized solar cells, *Electrochim. Acta*, 2014, **133**, 174–179, DOI: 10.1016/j.electacta.2014.04.010.

64 C. G. Fotsop, A. Lieb and F. Scheffler, Core-shell material based on ion-exchange-assisted growth of ZIFs on chamfered-edged zeolite crystals for N_2/CO_2 adsorption: Modeling and mechanism, *J. Environ. Chem. Eng.*, 2025, **13**(6), 119887, DOI: 10.1016/j.jece.2025.119887.

65 C. G. Fotsop, A. Lieb and F. Scheffler, Core-satellite material based metal-doped zeolite LTA for highly efficient iodine sequestration: Adsorption performance and mechanism, *Inorg. Chem. Commun.*, 2026, **183**, 115742, DOI: 10.1016/j.inoche.2025.115742.

66 X. Du, W. Fu and P. Su, *et al.*, Trace FeCu@PC Derived from MOFs for Ultraefficient Heterogeneous Electro-Fenton Process: Enhanced Electron Transfer and Bimetallic Synergy, *ACS EST Eng.*, 2021, **1**(9), 1311–1322, DOI: 10.1021/acsestengg.1c00131.

67 A. R. Dhahawi Ahmad, S. S. Imam and W. D. Oh, *et al.*, Fe_3O_4-Zeolite Hybrid Material as Hetero-Fenton Catalyst for Enhanced Degradation of Aqueous Ofloxacin Solution, *Catalysts*, 2020, **10**(11), 1241, DOI: 10.3390/catal10111241.

68 Z. Li, J. Lyu and M. Ge, Synthesis of magnetic Cu/$CuFe_2O_4$ nanocomposite as a highly efficient Fenton-like catalyst for methylene blue degradation, *J. Mater. Sci.*, 2018, **53**(21), 15081–15095, DOI: 10.1007/s10853-018-2699-0.

69 M. Wang, G. Fang and P. Liu, *et al.*, Fe_3O_4@β-CD nanocomposite as heterogeneous Fenton-like catalyst for enhanced degradation of 4-chlorophenol (4-CP, *Appl. Catal., B*, 2016, **188**, 113–122, DOI: 10.1016/j.apcatb.2016.01.071.

70 T. G. Merlain, L. T. Nanganoa and B. B. P. Desire, *et al.*, Fenton-Like Oxidation of Acid Yellow 23 in the Presence of Iron Rich Soil, *ACES*, 2016, **06**(05), 553–569, DOI: 10.4236/aces.2016.65048.

71 T. G. Merlain, D. Kouatou and N. J. Nsami, *et al.*, An efficient heterogeneous Fenton catalyst based on modified iron rich soil for discoloration of Tartrazine simulated wastewater, *J. Appl. Surf. Interfaces*, 2019, **5**(13), DOI: 10.48442/IMIST.PRSM/JASI-V5I1-3.15904.

72 M. Dolatabadi, A. Ghorbanian and S. Ahmadzadeh, Degradation of High-Concentration of Perchloroethylene from Aqueous Solution Using Electro-Fenton Process, *J. Environ. Health Sustain. Dev.*, 2022, **7**(2), DOI: 10.18502/jehsd.v7i2.9790.

73 J. J. Pignatello, E. Oliveros and A. MacKay, Advanced Oxidation Processes for Organic Contaminant Destruction Based on the Fenton Reaction and Related Chemistry, *Crit. Rev. Environ. Sci. Technol.*, 2006, **36**(1), 1–84, DOI: 10.1080/10643380500326564.

74 M. Moosavifar, S. M. Heidari and L. Fathyunes, *et al.*, Photocatalytic Degradation of Dye Pollutant Over FeTPP/NaY Zeolite Nanocomposite, *J. Inorg. Organomet. Polym.*, 2020, **30**(5), 1621–1628, DOI: 10.1007/s10904-019-01277-y.

75 L. Wang, B. Li and D. D. Dionysiou, *et al.*, Overlooked Formation of H_2O_2 during the Hydroxyl Radical-Scavenging Process When Using Alcohols as Scavengers, *Environ. Sci. Technol.*, 2022, **56**(6), 3386–3396, DOI: 10.1021/acs.est.1c03796.

76 A. K. Shimi, C. Parvathiraj and S. Kumari, *et al.*, Green synthesis of SrO nanoparticles using leaf extract of *Albizia julibrissin* and its recyclable photocatalytic activity: an eco-friendly approach for treatment of industrial wastewater, *Environ. Sci.: Adv.*, 2022, **1**(5), 849–861, DOI: 10.1039/D2VA00018K.

77 H. Kaur, A. Sharma and K. Anand, *et al.*, Green synthesis of ZnO nanoparticles using E. cardamomum and zinc nitrate precursor: a dual-functional material for water purification and antibacterial applications, *RSC Adv.*, 2025, **15**(21), 16742–16765, DOI: 10.1039/D5RA01469G.

78 X. Gao, Q. Guo and G. Tang, *et al.*, Effects of inorganic ions on the photocatalytic degradation of carbamazepine, *J. Water Reuse Desalin.*, 2019, **9**(3), 301–309, DOI: 10.2166/wrd.2019.001.

79 C. Wang, L. Zhu and M. Wei, *et al.*, Photolytic reaction mechanism and impacts of coexisting substances on photodegradation of bisphenol A by Bi_2WO_6 in water, *Water Res.*, 2012, **46**(3), 845–853, DOI: 10.1016/j.watres.2011.11.057.

80 Y. Wang, K. Lu and C. Feng, Influence of inorganic anions and organic additives on photocatalytic degradation of methyl orange with supported polyoxometalates as photocatalyst, *J. Rare Earths*, 2013, **31**(4), 360–365, DOI: 10.1016/S1002-0721(12)60286-5.

81 C. E. Onu, J. T. Nwabanne and P. E. Ohale, *et al.*, Comparative analysis of RSM, ANN and ANFIS and the mechanistic modeling in eriochrome black-T dye adsorption using modified clay, *S. Afr. J. Chem. Eng.*, 2021, **36**, 24–42, DOI: 10.1016/j.sajce.2020.12.003.

82 A. Abubakar, M. Manogaran and H. M. Yakasai, *et al.*, Response Surface Method for the Optimization of E. cloacae Strain UPM2021a Growth on Acrylamide as a Nitrogen Source, *Bioremed. Sci. Technol. Res.*, 2022, **10**(2), 29–39, DOI: 10.54987/bstr.v10i2.779.

83 M. Amarzadeh, M. Azqandi and K. Nateq, *et al.*, Heterogeneous Fenton-like Photocatalytic Process towards the Eradication of Tetracycline under UV Irradiation: Mechanism Elucidation and Environmental Risk Analysis, *Water*, 2023, **15**(13), 2336, DOI: 10.3390/w15132336.

84 R. Antón-Herrero, C. García-Delgado and M. Alonso-Izquierdo, *et al.*, Comparative adsorption of tetracyclines on biochars and stevensite: Looking for the most effective adsorbent, *Appl. Clay Sci.*, 2018, **160**, 162–172, DOI: 10.1016/j.clay.2017.12.023.

85 C. Wang, R. Sun and R. Huang, *et al.*, Superior Fenton-like degradation of tetracycline by iron loaded graphitic carbon derived from microplastics: Synthesis, catalytic performance,

and mechanism, *Sep. Purif. Technol.*, 2021, **270**, 118773, DOI: 10.1016/j.seppur.2021.118773.

86 N. Vân-Anh, B. B. Canh and C. H. Ha, Effect of Key Parameters on Heterogeneous Fenton-Like Oxidation of Indigo Carmine Catalyzed by $Fe_2V_4O_{13}$, *JST: ETSD*, 2023, **33**(4), 008–016, DOI: 10.51316/jst.169.etsd.2023.33.4.2.

87 A. S. Eltaweil, A. M. Galal and E. M. Abd El-Monaem, *et al.*, Enhanced Fenton Degradation of Tetracycline over Cerium-Doped MIL88-A/g-C_3N_4: Catalytic Performance and Mechanism, *Nanomaterials*, 2024, **14**(15), 1282, DOI: 10.3390/nano14151282.

88 B. Barikbin, F. S. Arghavan and A. Othmani, *et al.*, Degradation of tetracycline in Fenton and heterogeneous Fenton like processes by using $FeNi_3$ and $FeNi_3/SiO_2$ catalysts, *Desalin. Water Treat.*, 2020, **200**, 262–274, DOI: 10.5004/dwt.2020.26061.

89 J.-B. Tarkwa, E. Acayanka and B. Jiang, *et al.*, Highly efficient degradation of azo dye Orange G using laterite soil as catalyst under irradiation of non-thermal plasma, *Appl. Catal., B*, 2019, **246**, 211–220, DOI: 10.1016/j.apcatb.2019.01.066.

90 K. V. Kumar, K. Porkodi and F. Rocha, Langmuir–Hinshelwood kinetics – A theoretical study, *Catal. Commun.*, 2008, **9**(1), 82–84, DOI: 10.1016/j.catcom.2007.05.019.

91 O. O. Balayeva, Photocatalytic degradation of Ponceau 4R by ZnAl -layered double hydroxide nanostructures obtained with and without polyvinyl alcohol, *J. Chin. Chem. Soc.*, 2022, **69**(9), 1594–1607, DOI: 10.1002/jccs.202200121.

92 M. Mahajan, S. Kumar and J. Gaur, *et al.*, Green synthesis of ZnO nanoparticles using *Justicia adhatoda* for photocatalytic degradation of malachite green and reduction of 4-nitrophenol, *RSC Adv.*, 2025, **15**(4), 2958–2980, DOI: 10.1039/D4RA08632E.

93 D. Jalandhara, S. Kumar and J. Dalal, *et al.*, A multifunctional Co-doped $BiFeO_3$ nanocomposite: a promising candidate for photocatalytic degradation, antibacterial activity, and antioxidant applications, *Mater. Adv.*, 2025, **6**(2), 641–657, DOI: 10.1039/D4MA01053A.